

The Nature of Radio Emission from Distant Galaxies: The 1.4 GHz Observations

E. A. Richards

National Radio Astronomy Observatory¹ and University of Virginia

Received _____; accepted _____

arXiv:astro-ph/9908313v1 27 Aug 1999

¹The National Radio Astronomy Observatory is a facility of the National Science Foundation operated under cooperative agreement by Associated Universities, Inc.

ABSTRACT

We have conducted a deep radio survey with the Very Large Array at 1.4 GHz of a region containing the Hubble Deep Field. This survey overlaps previous observations at 8.5 GHz allowing us to investigate the radio spectral properties of microjansky sources to flux densities greater than $40 \mu\text{Jy}$ at 1.4 GHz and greater than $8 \mu\text{Jy}$ at 8.5 GHz. A total of 371 sources have been catalogued at 1.4 GHz as part of a complete sample within $20'$ of the HDF. The differential source count for this region is only marginally sub-Euclidean and is given by $n(S) = (8.3 \pm 0.4)S^{-2.4 \pm 0.1} \text{ sr}^{-1}\text{Jy}^{-1}$. Above about $100 \mu\text{Jy}$ the radio source count is systematically lower in the HDF as compared to other fields. We conclude that there is clustering in our radio sample on size scales of $1'$ - $40'$.

The 1.4 GHz selected sample shows that the radio spectral indices are preferentially steep ($\bar{\alpha}_{1.4} = 0.85$) and the sources are moderately extended with average angular size $\theta = 1.8''$. Optical identification with disk-type systems at $z \sim 0.5$ - 0.8 suggests that synchrotron emission, produced by supernovae remnants, is powering the radio emission in the majority of sources. The 8.5 GHz sample contains primarily moderately flat spectrum sources ($\bar{\alpha}_{8.5} = 0.35$), with less than 15% inverted. We argue that we may be observing an increased fraction of optically thin bremsstrahlung over synchrotron radiation in these distant star-forming galaxies.

Subject headings: galaxies: evolution – galaxies: active – galaxies: starburst – cosmology: observations – radio continuum: galaxies

1. Introduction

Deep radio surveys show a surface density of radio objects approaching 60 arcmin^{-2} down to $1 \mu\text{Jy}$ (as inferred from fluctuation analyses on the most sensitive VLA images at 1.4 and 8.4 GHz), or equal to the surface density of $B = 27$ magnitude galaxies (Fomalont *et al.* 1991, Windhorst *et al.* 1993, Richards 1996, Richards *et al.* 1998, hereinafter Paper I). Despite their modest average luminosity of $L \simeq 10^{22.5} \text{ W/Hz}$, the sheer number of microjansky sources implies that they dominate the radio luminosity budget of the universe at centimeter wavelengths. However, surprisingly little is known about the physical origin of these objects or their nature.

Some generalizations from studies involving deep 5 and 8.5 GHz VLA fields imaged with HST and ground-based telescopes are possible (Hammer *et al.* 1995, Windhorst *et al.* 1995, Fomalont *et al.* 1997, Richards *et al.* 1998). At least half of microjansky sources are associated with morphologically peculiar, merging and/or interacting galaxies with evidence for active star-formation (blue colors, infra-red excess, HII-like optical spectra). The remaining identifications are composed of low-luminosity FR Is, ellipticals, Seyferts, LINERs, and luminous star-forming field spirals. Thus a variety of physical mechanisms may be driving the observed evolution among microjansky radio sources, including non-thermal radiation from AGN activity, synchrotron emission associated with diffuse supernova remnants, and thermal emission from HII regions.

Another clue is available from the observed distribution of radio spectral indices. While at millijansky levels, the average spectral index for radio sources is about $\alpha \sim 0.8$ (Donnelly *et al.* 1987), microjansky sources selected at high frequencies ($\nu \geq 5 \text{ GHz}$) have a surprisingly flat spectra of $\alpha = 0.3 \pm 0.2$ (Fomalont *et al.* 1991, Windhorst *et al.* 1993). Several explanations for this observed flattening compared with sources selected at higher flux density levels are possible, including, free-free absorption, an increasing number

of synchrotron self-absorbed AGN among the microjansky population, and/or a rising component of thermal radiation from active star-formation.

The purpose of this study is to enlarge the faint radio sample and investigate the radio spectral and morphological properties for a statistically significant sample of microjansky sources. In addition, examination of the optical properties of the identifications may shed insight into the nature of the radio emission in these sources. To further this goal we have observed a region of the sky at 1.4 GHz and 8.5 GHz centered on the Hubble Deep Field, where excellent wide field optical data are available. In Paper I (Richards et al. 1998) we presented the optical identifications for a complete sample of twenty-nine 8.5 GHz selected radio sources in our radio survey of the Hubble Deep Field. The principal conclusion is that the majority ($\sim 70\%$) of the identifications are with relatively bright ($R \sim 22$ mag.) disk systems, many at moderate redshifts ($z = 0.4-1$). In this paper (Paper II) we present the 1.4 GHz observations. In section two we describe our observations and data reduction techniques. Section three presents our source list, while in section four we calculate the spectral index distribution. In §5 we discuss the spatial clustering of sources in our catalog. Finally, in §6 we summarize our findings and give conclusions.

2. The 1.4 GHz Radio Observations and Data Reduction

In November 1996, we observed a field centered on the Hubble Deep Field ($\alpha = 12^h 36^m 49.4^s$ and $\delta = 62^\circ 12' 58.00''$ (J2000)) for a total of 50 hours at 20 cm in the A-configuration of the VLA. In order to minimize chromatic aberration, we observed in a pseudo-continuum, spectral line mode with 7×3.125 MHz channels centered on intermediate frequencies 1365 MHz and 1435 MHz, frequency windows known to be relatively free of radio frequency interference. Each frequency channel was composed of two independent circular polarizations. All knowledge of linear-polarized intensities was lost

due to the limited number of VLA correlator channels. Visibility data were recorded every 3.3 sec from the correlator.

We monitored the point source 1313+675 ($S_{1.4} = 2.40$ Jy), located 6.5 degrees from the HDF, every 40 minutes to provide amplitude, phase, and bandpass calibration. Daily observations of 3C286 with assumed flux densities of 14.91 Jy at 1385 MHz and 14.62 Jy at 1435 MHz provided the absolute flux density scale.

The calibrator observations allowed us to identify baselines with systematic phase or amplitude errors. A few baselines were found to have recurrent amplitude and/or phase closure errors greater than five percent and/or five degrees. All data associated with these suspicious baselines were discarded. To remove bursts of radio frequency interference, we excised all visibilities with flux densities greater than about 10σ above the expected rms value of 0.08 Jy. This amounted to about 2% of the data.

After time averaging the (u, v) data from 3.3 to 13 sec, we made preliminary $10''$ resolution maps which cover the field out to the first sidelobe of the primary beam about 0.8° from the phase center. We searched these images for bright, confusing sources whose sidelobes might contaminate the noise properties of the inner portion of field. All sources above 0.5 mJy were catalogued.

We then imaged and heavily CLEANed these sources using the full unweighted (u, v) data set. Because the primary beam response changes significantly over our 44 MHz bandpass (about 3%), it was necessary to deconvolve each of the confusing sources using each 3.125 MHz channel. In addition, the confusing sources were independently deconvolved in each of the circular polarizations (right and left) to account for the 'beam squint' of the VLA antenna. Their CLEAN components were Fourier transformed and then subtracted from the visibility data. Using these "strong source subtracted data sets", we then imaged the inner few arcmin of the field. With this procedure the rms noise was found to be about

50% higher than expected from receiver noise alone. In particular, a few sidelobes from particularly strong sources ($S > 10$ mJy) located near the half power point and first null of the primary beam were still apparent.

By examining the images made from 30 minute segments of the data, we isolated a few time intervals where the visibility data appeared to be corrupted, possibly due to low level interference. For any of these 30 minute snap-shot images with a rms noise greater than 50% of the mean value, the corresponding visibility data were deleted from the final analysis. These data amounted to about seven hours of time; thus, in all, about 42 hours of high quality data were used to construct the final images. The final combined data set has a rms noise of $7.5 \mu\text{Jy}$, whereas we expected a noise closer to $5 \mu\text{Jy}$.

2.1. Construction of the 1.4 GHz Images

Our goal is to map the $40'$ field of the 1.4 GHz observations out to the 20% response of the VLA antennas. There are two complications which make this a difficult task.

First is the sky curvature. While in practice the VLA is often treated as a two dimensional array, in reality the instrumental response to radio emission from the sky is a three dimensional complex function. For observations of short duration, small fields of view, or low resolution, most sources can be adequately deconvolved without reference to the so called 3-D effect. However, the isoplanic assumption fails for sources located further than $\theta \simeq 1/n_{syn}$ radians from the phase tracking center, where n_{syn} is the phase center distance in synthesized beam widths. For the A-array at 1.4 GHz this corresponds to a patch size of about 18 arcmin across.

Thus we chose to approximate the one degree primary beam of our observations by using a number of independent and equidistant facet images. Each facet is constructed from

the Fourier transform of the data which has been phase shifted to its tangent point on the celestial sphere. In all, 16 facets were used. This technique is known as polyhedral imaging and is discussed at length by Cornwell & Perley (1992).

One further complication comes from the practical limitation of the extensive computations needed to reduce these wide field observations. Our entire calibrated and edited data set consists of over 10^7 discrete complex visibilities (after 13 sec time averaging) which must be directly Fourier transformed to compute the sky brightness distribution over approximately the same number of pixels. Because we are interested in radio emission over the entire primary beam, we must properly deconvolve sources within the entire field of view. Although only sources fainter than 0.5 mJy remain in the visibility data after the subtraction of the confusing sources, their collective sidelobes can limit the dynamic range of the final images.

The most accurate method for deconvolution of the faint sources is to CLEAN each of the 16 images in parallel, subtracting each source's sidelobe contribution from all the image facets simultaneously. In this manner, one would recover the sky brightness function free from sidelobe contamination over the entire primary beam. However, in practice, this is a prohibitive computational task. Therefore we opted to CLEAN each of the 16 facets in series using the much more efficient Clark-Hogbom algorithm (Clark 1980). The price paid is that sidelobes from the multitude of sources less than 0.5 mJy are only properly removed locally, within the individual image facet which contains each source.

In order to examine what effect this might have on the rms noise near the center of the image, we performed a simple test. First we made an image of the inner seven arcmin of the field center, heavily CLEANed using the Clark-Hogbom method. Then we made a similar image twice the size of the former, again heavily CLEANed. Comparison of the two images, one relatively free of sidelobe contamination from the far field sources with $S \leq 0.5$

mJy, the other not, yields a first order approximation of the unCLEANed sidelobes left in the center of the field due to our deconvolution method outlined above. About $0.8 \mu\text{Jy}$ of flux density remains per independent beam, and thus increases the noise about 10% over the thermal noise.

We produced the final image by CLEANing each of the sixteen 2048×2048 pixel fields ($0.4''$ pixels) with 10,000 iterations and a 10% loop gain. This produced an image with a natural resolution of $2.0'' \times 1.8''$ and P. A. = -86° . The rms noise near the center of the field was $7.5 \mu\text{Jy}$, approximately 30% higher than the value expected from thermal noise alone based on our system temperature (37 K on average), integration time, and bandwidth. The noise in each of the 16 images was found to be fairly uniform, although it increased to as much as $10 \mu\text{Jy}$ in regions near the brightest millijansky sources.

Residual ringlike structure from unCLEANable sidelobes around these strong sources was evident, suggesting that our images are dynamic range limited at about 5000:1. This is typical of blank field deep imaging where the data cannot be effectively self-calibrated. We clipped out regions immediately around these sources, as well as a larger region around one particularly strong source ($S = 35 \text{ mJy}$) located at the half-power point of the primary beam. We attribute the dynamic range limitation in this image to pointing fluctuations, which are typically $15''$ rms for the VLA. This effect causes amplitude fluctuations in the apparent brightness of the radio sources, which are of order 1% at the half power point, and hence induces unCLEANable sidelobes into the image.

Examination of the stronger deconvolved sources in the field with $S_p \gtrsim 5 \text{ mJy}$ showed evidence of a radial sidelobe oriented towards the phase tracking center, or center of our images. These sidelobes appeared to be symmetric about these stronger millijansky sources in the field and with first order amplitude of about 10%. Their width was approximately that of the delay beam.

These sidelobes were also apparent during our test observations of 1400+621, and only appear around the off axis observations. Other observations taken at the VLA have not shown similar artifacts and our suspicion is that the problem was an online system recording error with the 3.3 sec visibility data that we chose to use. Examination of VLA data of the same test field taken in an identical observing mode, except with 10 sec visibility integration, showed no sign of the radial sidelobes.

The cause of these artifacts is unknown. They do not appear to be present around the near field, weaker sources (less than about 1 mJy). As a test of whether these sidelobes might adversely effect our measurements of the flux densities of the stronger millijansky sources, we examined the off-axis flux density measurements of 1400+621 in images with and without the presence of the radial sidelobes. The measurements agree to within the standard flux density errors. It is more difficult to assess if these radial sidelobes adversely affect the general rms noise in the final 1.4 GHz images.

3. The Complete Source List

In order to minimize the introduction of spurious radio sources into our sample, we examined the distribution of the *negative* pixels in the images to estimate its completeness limit. In general most regions appeared to reflect well behaved Gaussian noise with the most negative peak being about five times the local rms noise. However, one region with a local rms of $7.5 \mu\text{Jy}$ contained an unresolved negative feature with $S_p = -63 \mu\text{Jy}$. This feature appeared to be quite isolated and located several arcmin from any of the brighter millijansky confusing sources. No other strange artifacts (e.g., rings, streaks, residual sidelobes) were apparent in the vicinity of this negative 'source'; hence its presence remains enigmatic. The next most negative pixel value of $-40 \mu\text{Jy}$ is located near a strong confusing source. We therefore adopt $40 \mu\text{Jy}$ to be the formal completeness limit over our entire one

degree field. Even if there are positive counterparts to the $-63 \mu\text{Jy}$ 'source', there should be no more than a few if the negative and positive pixel amplitude distribution are fairly symmetric about zero. However, we note that the probability of finding a -9σ source within our field is much less than one percent, and demonstrates that the noise properties of this image are not entirely Gaussian.

Next we searched our images for all pixels with $S \geq 40 \mu\text{Jy}$ and fit these sources with elliptical Gaussians to determine their peak flux densities and positions using the automated AIPS task SAD. In all 314 sources were found within 20 arcmin of the center of the image (20% power contour).

3.1. Determination of Discrete Source Angular Sizes and Flux Densities

Gaussian fitting routines such as SAD are subject to noise dependent biases which cause significant overestimation of source sizes and flux densities (Windhorst et al. 1984, Condon 1997). In order to estimate the effects of population and noise bias in our images, we performed a series of Monte Carlo simulations. Our basic technique was to inject a number of point sources (100) of known flux density into the CLEANed sky images of this field. Then these sources were recovered from the images using SAD and their measured peak and integrated flux densities compared to the input model. We used the ratio S_p/S_i to determine if the simulated source was significantly broadened by population and/or noise bias.

Because our goal is to set a resolution criteria in the presence of these fitting biases, we performed this simulation as a function of flux density, or alternatively, signal to noise. By examining the distribution of S_p/S_i at different flux densities, we obtained some idea about at what level we could confidently believe that a given source was resolved in our real

sky images. For a source of intrinsic dimension $\theta_{maj} \times \theta_{min}$ resolved by a beam of extent $a_{maj} \times a_{min}$, the integrated and peak flux densities are related by $S_i = S_p(1 + \frac{\theta_{maj} \times \theta_{min}}{a_{maj} \times a_{min}})$, thus allowing us to relate the ratio S_p/S_i directly to a source angular size. By examining the distribution of modeled S_p/S_i to input S_p/S_i , we were able to adopt a 95% confidence in the resolution criteria as a function of signal to noise. The resulting best fit data yields S_p/S_i (95%) $< 1 - \frac{2.3}{\sigma_{snr}}$ where σ_{snr} is the signal to noise ratio of the radio source. Thus at the detection limit of our images (40 μ Jy), a source must have a S_p/S_i value less than 0.57 to satisfy our resolution criterion, or an angular size greater than about 2.7". It follows that we can resolve only those sources stronger than 70 μ Jy integrated flux in our complete sample.

Next, we used these same simulations with the sources of angular size that we could have just detected at each signal to noise ratio (e.g., 2.7" at $S_p = 40$ μ Jy). Comparison of the input to recovered peak and integrated flux densities, and angular sizes yields an estimate of the bias induced by Gaussian fitting techniques in the presence of population and noise bias. We corrected our real sky source parameters to account for these biases. In general the peak flux densities of the fitting routines were in good agreement with the models, while the integrated flux densities and angular sizes from the Gaussian fits were overestimated by up to a factor of 1.5.

As a check on the integrated flux densities for apparently resolved sources in our complete sample obtained from the Gaussian fitting algorithms, we examined the distribution of peak flux densities as measured in various resolution images. Images were constructed at 1", 3.5", and 6" resolution in addition to our nominal 2" naturally weighted image. Table 1 gives the parameters of each image. For those sources which satisfied our initial resolution criterion, we checked that the peak flux density of the source increased with decreasing resolution consistent with the fitted angular size. Those sources which did

not were considered unresolved and their adopted peak and integrated flux densities were measured on the the 2'' image. Figure 1 shows a greyscale of the inner 10' of the 1.4 GHz image. In Figure 2, we show the greyscale of the 8.5 GHz mosaic image (see §6).

We also searched the lower resolution 3.5'' and 6'' images for resolved sources not detected in the untapered 2'' image above our completeness limit of $S_p = 40 \mu\text{Jy}$. This search yielded 57 additional sources in the tapered images above completeness limits of 50 μJy at 3.5'' resolution and 75 μJy at 6'' resolution. Because the angular sizes are uncertain in these low signal to noise ratio detections (and in many cases may be instrumentally broadened), the adopted peak and integrated flux densities were set equal to the peak pixel values in the tapered images. These additional sources were added to the complete source list which in total contains 371 sources. The complete sample of all radio sources detected at 1.4 GHz within 20' of the phase center is presented in Table 2.

A description of Table 2 is as follows. All uncertainties are given at the one sigma level.

Column (1) — The Right Ascension in J2000 coordinates with one sigma uncertainty.

Column (2) — The Declination in J2000 coordinates with one sigma uncertainty.

Column (3) — The *deconvolved* (FWHM) major axis of the best Gaussian fit to the source, Θ , is given in arcsec.

Column (4) — The signal to noise ratio of the detection calculated from S_p/σ where S_p is the peak flux density as measured in either the 2'', 3.5'', or 6'' image, and σ equals the rms noise in that image.

Column (5) — The integrated sky flux density ($S_{1.4}$) after correction for the instrumental gain, (see §3.2),

with corresponding one sigma errors.

3.2. Instrumental Corrections

We must also correct the derived source parameters for various instrumental effects. In order to measure the off axis response of the VLA to a point source, we observed the 4.2 Jy point source 1400+621 in each of the cardinal directions at positions of 5, 10, 15, 20 and 25 arcmin from the nominal phase reference center.

There are four principal effects which reduce point source response as a function of radial distance from the phase center. In their degree of increasing importance they are 1) 3-D smearing, 2) finite time visibility sampling (time delay smearing), 3) chromatic aberration (bandwidth smearing), and 4) primary beam attenuation.

1. We have approximated the curvature of the celestial sphere with a number of two-dimensional facets. However, smearing may still be present at a reduced level near the edges of each of our individual facet images. The effect of a small amount of 3-D smearing are such that the integral flux density of a given source is preserved while its peak signal is reduced by an amount dependent on distance from the tangent point on the celestial sphere. In order to determine the amplitude of 3-D smearing in our data, we performed a series of simulations inserting point sources at a variety of distances from the phase tracking center into visibility data with our exact (u, v) coverage. These data were then imaged in the same manner as the true sky images. In this manner we determined the amount of point source degradation as a function of distance from the celestial sphere tangent point or image facet center. At the maximum possible distance of a source from a tangent point ($\sim 600''$) the peak degradation is less than 20%. All values of the peak flux density (S_p) were corrected for this effect according to our empirically fit polynomial.

2. The calibrated (u, v) data set used to construct our images consisted of 13 sec averaged visibility data. Because the actual radio sources rotate in the sky during this sampling time, their flux density is smeared in the image plane. The analytic calculation

of this smearing is complicated by the aspects of the observing geometry. However, at the North Celestial Pole the effect reduces to a tangential smearing in the image plane and its amplitude is given by $S_p/S_t = 1 - 2.06 \times 10^{-9} \theta/\theta_{syn}$ where S_t is the integrated flux density of a source located an angular distance θ from the phase tracking center and θ_{syn} is the size of the synthesized beam. We used this approximation to correct the peak flux densities as measured in our images.

3. Although we planned our observations of the HDF field to minimize the effects of chromatic aberration, for far-field sources this effect can still be important. It is especially crucial to understand the effects of smearing on the completeness level of the images. We measured the off-axis response of 1400+621 due to chromatic aberration by examining the ratio of the peak to integrated flux density, S_p/S_i , as a function of distance from the image phase center. Bandwidth smearing is governed by the observing frequency, width and shape of the bandpass and the (u, v) coverage, all of which define the synthesized beam. In theory, these are known functions and the final beam response can be calculated analytically as a function of position in the image. However, in practice such uncertainties as non-uniform (u, v) coverage, central intermediate frequency offsets, and imperfect bandpass filters make this impossible. We chose instead to fit a function to the empirical data of the form $S_p/S_i = (1+(r/k)^2)^{-0.5}$ where r is the distance from the phase center and k is a constant which absorbs the uncertainties discussed above. Our least squares fit to the empirical data is shown in Figure 3 where $k = 16.19$ arcmin. This is within 3% of the theoretical value assuming $\delta\nu/\nu = 3.125/1400.5$ and a $\theta_{beam} = 2.1''$. For purposes of correcting S_p in our images, we use the above equation scaled by the appropriate beam size. The integrated flux density, S_i is preserved and needs no correction for smearing.

4. The primary beam attenuation at 1.40 GHz has been measured to about 1% (Condon 1997) to the first sidelobe (-10 dB). Each of the peak and integrated flux densities

in the source list were corrected for the primary beam attenuation. The uncertainty in the correction is the standard rms pointing error of the VLA elements (about $15''$) multiplied by the differential log of the primary beam response.

In Figure 3 we plot the point source response of a source as a function of distance from the phase center. We define the instrumental gain factor as the product of bandwidth smearing, time averaging smearing, and the primary beam correction.

3.3. Positional Accuracy

The assumed position of our phase calibrator 1400+621 is $\alpha = 14^h00^m28.6526^s$ and $\delta = 62^\circ15'38.526''$ (J2000). We observed systematic, monotonically increasing shifts in both RA and DEC of comparable amplitude as a function of r . It is a small effect and the difference between the actual radial distance from the field center and that measured in the image plane is $\delta r = -0.042$ arcsec at 25 arcmin distance from the field center.

This small systematic term can be explained by the so called annual aberration effect (Fomalont et al. 1992). The predicted scale contraction from annular aberration in the direction of the HDF during the Julian epoch 1996.6 is 0.9999783. The good agreement between the observed and predicted scaling factor for 1400+621 yields confidence that our images are free from significant distortions due to asymmetric bandpasses or IF offsets.

We also corrected all the radio source positions in our catalog for position offsets induced by the 3-D effect as discussed in §3.2. By phase shifting the image tangent points to the location of individual sources, their true angular positions on the sky were measured. The difference between the apparent position as measured on the nominal sky maps and the corrected positions is typically only $0.2''$ in the north-south direction.

After correction for annular aberration and the 3-D term, the relative positional

accuracy for sources across the field in the limit of infinite signal to noise should approach about $0.02''$. The absolute positional accuracy depends on the translation of our phase calibrator position to that of the HDF and is about $0.02''$. Thus we estimate our radio catalog to be within $0.03''$ of the J2000/FK5 coordinate grid. The single coordinate rms position errors as given in Table 2 are defined as $\sigma = \sqrt{(1.8''/2\sigma_{snr})^2 + (0.03'')^2}$.

4. Survey Completeness and Source Counts

Because the completeness of the radio source sample is defined in terms of peak image flux, S_p , corrections must be made for the the instrumental response and biases inherent in our detection algorithm. Although we have corrected the individual sources in Table 2 for these effects, we now calculate the fraction of sky sources which remain undetected in our survey due to the finite angular size of the sources.

4.1. Angular Size Distribution

Previous high resolution studies of the microjansky radio population suggested that the median angular size (θ_{med}) for submillijansky radio sources is approximately $2''$ and almost independent of flux density between 80 - 1000 μJy (Windhorst et al. 1993, Fomalont et al. 1991, Oort 1988). The resolution of our present microjansky survey is thus well suited to study the angular size distribution for a statistically large and well defined sample of microjansky radio sources.

Of the 151 radio sources in our complete sample with $70 \mu\text{Jy} < S_i < 1000 \mu\text{Jy}$ for which we have angular size information, only 77 (50%) are resolved with our typical $2''$ resolution limit. We divided these sources into two flux density bins, containing approximately equal numbers of resolved sources. Considering only the number of radio sources with angular

size greater than $2.7''$ (the angular size detection limit of the weakest radio sources in our sample as defined in §3.1), we find twice as many resolved sources with $S_i > 250 \mu\text{Jy}$ (52%) as opposed to those with $S_i \leq 250 \mu\text{Jy}$ (25%). This suggests that θ_{med} may be a *decreasing* function of flux density. Figure 4 shows our measurements of angular size as a function of source intensity. In order to estimate the mean angular size of this sample, we applied the survival analysis techniques of Feigelson & Nelson (1985) using the statistical package ASURV (Rev. 1.2; Isobe & Feigelson 1992). This technique incorporates upper limits in the calculation of the mean of a distribution, which is particularly important in our sample which is dominated by non-detections (i.e. we are measuring the tail of the angular size distribution). The technique assumes a symmetric Gaussian model, hence the mean and median are equal. At $S_{1.4} = 370 \mu\text{Jy}$, $\theta_{med} = 2.6'' \pm 0.4''$, and at $S_i = 100 \mu\text{Jy}$, $\theta_{med} = 1.6'' \pm 0.3''$. The errors are based on the number of angular size measurements (not limits).

In Fig. 5, we compare our determinations of θ_{med} with previous measurements made at 1.4 GHz. Because of the uncertain selection effects inherent in the higher frequency deep radio surveys, particularly their bias towards flat-spectrum, compact AGN, we chose not to include these points. With the notable exception of the discrepant Condon & Coleman (1985) point, there is general agreement amongst the different data. Because the median angular size is known to change rather sharply below a few millijansky at 1.4 GHz (presumably due to the emergence of an increasing population of starburst galaxies among radio sources) from $\sim 10''$ to a few arcsec, we suggest that the high flux density point of Oort (1988) is too low, possibly due to resolution biases in his A-array snapshots.

We believe the decrease in angular size at lower flux densities to be real. Thus for the purposes of modeling the median angular size-flux density relationship, we fit a function of the form:

$$\theta = \text{frac}34 \times 0.175 S_{1.4}^{0.5} + \text{frac}14 \times 0.1 \text{ arcsec}$$

This fit is also shown in Fig. 5. For completeness, we also plot a straight line, with $\theta = 2.0''$ and independent of flux density.

4.2. Completeness

In order to investigate the combined effects of noise, population, and resolution bias on the completeness level of our survey, we used a series of Monte Carlo simulations similar to the ones described in §3.1. In particular we want to determine how many sources with $S_i \geq 40 \mu\text{Jy}$, but with $S_p < 40 \mu\text{Jy}$ we missed based on our peak flux density detection limit. We randomly populated our sky images with 100 sources of finite angular size assuming an angular size distribution as found in §4.1. This simulation was repeated at a variety of flux densities from 40 to 1000 μJy . In each flux density interval the ratio of the number of sources recovered from the images with $S_p \geq 40 \mu\text{Jy}$ to the number originally injected in the model was tabulated. This was taken to be the effective correction factor needed to account for the combined effects of resolution, population and noise bias in our images (although resolution bias is always the dominant term). At 80 μJy which is the average flux density source detected in our survey (weighted by $S^{-2.4}$) and where the count will most accurately be determined, this correction factor is 1.05. As resolution bias is the dominant source of incompleteness in our survey, we estimate that we have detected approximately 95% of the microjansky sources in the HDF region to this flux density limit. The principal uncertainty in the correction factor is the uncertainty in the angular size distribution of the microjansky radio sources. If we had assumed a constant $\theta = 2.0''$ model, our corrections would have increased by over a factor of two.

From the complete source list of Table 2, we then binned sources in flux density intervals such that each bin had at least 50 radio sources (except for the highest flux density bin). The differential count was then calculated based on the number of sources in each bin

interval. Bandwidth smearing, time averaging smearing, and the primary beam response decreases the effective area over which a source of given S_p can be detected. Thus when counting the number of sources in each bin, care must be taken to weight the contribution of each source to the count by the effective area over which it could have been detected. This factor can be calculated by solving for the image radius where a source of amplitude S_p would have just been missed by our peak detection limit (Katgert 1973). Table 3 presents the differential source counts for our complete flux limited sample. The counts from this survey are compared to other microjansky surveys in Figure 6a and 6b (Mitchell & Condon 1985, Oort & Windhorst 1985, Hopkins *et al.* 1998) normalized to a Euclidean geometry $n/n_o = n(s)/S^{-2.5}$. In general the agreement is reasonable and in agreement with the errors and possible field to field variations. The best fit to the source counts in this field in the range 40 - 1000 μJy is $n(S) = (8.25 \pm 0.42)S^{-2.38 \pm 0.13} \text{ ster}^{-1} \text{ Jy}^{-1}$.

The counts in the HDF appear systematically lower than those of other fields above 100 μJy . This effect could be due either to 1) real field to field variations on the degree scale as a result of large-scale clustering of radio sources, or 2) survey incompleteness due to the finite angular size of the radio sources. Without complementary, low resolution observations, it is difficult to discriminate between these two possibilities. We note that if the mean angular size does not decrease significantly below 100 μJy , the radio sky will become forever naturally confused at the level of a few hundred nanojansky, perhaps providing a natural limitation to the sensitivity of the next generation of centimeter radio telescopes (Windhorst *et al.* 1993).

5. Spatial Clustering

In order to test for the presence of two dimensional spatial clustering among the radio sources in the Hubble Deep Field, we calculated the two-point correlation function for the

sources in Table 2. First, we compiled a table of angular separations by considering the separation of each individual source with all other sources in the catalog. These provide our DD estimate (Peebles, 1980). Next, we generated random catalogs of sources according to the source count of §4.2, and distributed randomly across a $40'$ VLA primary beam. The peak flux densities of these sources have been attenuated by the instrumental corrections discussed in §3.2. Angular pairs were calculated for these catalogs and form the basis of our RR measurement. We define the correlation function of our catalog to be $w(\theta) = DD/RR - 1$. The correlation function of our catalog on scales of $0'$ - $40'$ is presented in Table 4.

We calculated the errors in our clustering measurement by following the bootstrap method of Ling et al. (1986). These agree well with the Poissonian error estimate of $\delta w(\theta) = 1 + w(\theta))/N_{DD}$ where N_{DD} is the number of independent data pairs in a given bin. We find evidence for an excess of radio sources on scales of approximately 1 - $10'$, while on scales much larger than this there are fewer radio sources in our catalog than expected from a random distribution. Figure 7 shows the correlation function for radio sources in the HDF, compared to the correlation function of a somewhat shallower 1.4 GHz survey of Oort (1987) complete to $100 \mu\text{Jy}$. The amplitudes are comparable in the two separate surveys.

Spatial clustering at higher flux density levels and lower amplitudes has been reported by Cress et al. (1996) and Magliocchetti et al. (1998). More recently, Hopkins et al. (1999) claim fluctuations in field to field source counts at similar completeness levels to ours, possibly indicating the presence of large-scale radio source spatial variations. Thus it is plausible that there are both fewer radio sources in the HDF region than the average field, and that these sources are clustered on arcmin scales amongst themselves.

6. Radio Spectral Indices

The HDF has been observed previously with the VLA at 8.5 GHz to a one sigma sensitivity of $1.8 \mu\text{Jy}$ (Paper I). In June 1997 we observed the HDF region for an additional 40 hours at 8.5 GHz. We mosaiced an area defined by four separate pointings offset $2.7'$ from the center of the HDF (the half-power scale of the primary beam response) in each of the cardinal directions for about 10 hours duration each. The observing technique and data reduction are discussed in Paper I. The final combined 8.5 GHz images have an effective resolution of $3.5''$ and a completeness limit of $8 \mu\text{Jy}$. The sensitivity of this mosaic to sky emission is a sharp function of distance from the nominal pointing center because the observations were heavily weighted towards imaging the central HDF region.

Because the size of the VLA primary beam scales inversely with frequency, our sensitivity at 8.5 GHz is limited to the inner 6.6 arcmin (HWHM) of the 1.4 GHz field. This is the point where the maximum beam attenuation at 8.5 GHz is equal to 0.2 (while at 1.4 GHz the attenuation is only 0.9). Within this region there are 109 sources contained in the 1.4 GHz complete sample. We measured the 8.5 GHz flux density at the location of each of these sources. When a source was not clearly detected ($S_p < 3\sigma$ at 8.5 GHz), we calculated a conservative upper limit to its 8.5 GHz flux density equal to three times the rms noise corrected by the antenna gain. If a 1.4 GHz radio source had a peak flux value $3\sigma < S_p < 5\sigma$, its flux limit was taken as S_p also corrected by the primary beam. This ensures that our 1.4 GHz selected spectral index sample is complete and free from uncertain weak source biases. Based on this criteria, 30 sources from the 1.4 GHz sample had clear counterparts in the 8.5 GHz image. Using the 1.4 GHz and 8.5 GHz flux density values as measured in their respective $3.5''$ convolved images, we calculated individual spectral indices using the convention $S_\nu \propto \nu^{-\alpha}$. In the following discussion, steep spectrum sources are defined as those with $\alpha \geq 0.50$, while flat spectrum as those with $\alpha < 0.50$.

The 1.4 GHz to 8.5 GHz spectral index distribution of the 1.4 GHz selected sample is shown in Figure 8 (only those with meaningful lower limits, $\alpha \geq 0.50$ are shown for clarity). Because of the large number of spectral index limits for the 1.4 GHz sample (79/109), we chose to only consider those sources with $S_{1.4} > 100 \mu\text{Jy}$ when calculating the mean of the sample. The mean as calculated from both the detections and lower limits (using ASURV) for sources with $S_{1.4} > 100 \mu\text{Jy}$ is $\bar{\alpha}_{1.4} = 0.85 \pm 0.16$. For those sources with $S_{1.4} > 100 \mu\text{Jy}$ the fraction of steep spectrum sources is $\alpha = 0.62$. We also calculated the median of the spectral index distribution for the entire 1.4 GHz sample. We did not consider spectral index lower limits which were weaker than $\alpha_{1.4} > 0.3$, to avoid a bias in the median calculation. The median of the 1.4 GHz selected sample is 0.63.

We now consider those radio sources within the central $6.6'$ (HWHM) detected on the basis of the 8.5 GHz data alone. There are 29 sources in the complete sample 8.5 GHz sample of Paper I. Eleven additional sources were detected in the mosaiced regions with $S_p \geq 5\sigma$. These 40 sources comprise a complete sample of radio sources detected at 8.5 GHz within $6.6'$ of the HDF center. We measured the 1.4 GHz flux densities at their positions in the $3.5''$ image. All but 10 of these sources are contained in the complete 1.4 GHz sample in Table 2. Upper limits to the 1.4 GHz flux density were calculated as three times the rms normalized by the antenna gain.

The spectral index distribution is shown in Figure 9. The mean spectral index for the 8.5 GHz selected sample is $\bar{\alpha}_{8.5} = 0.35 \pm 0.07$ while the median spectral index of the detections is 0.41. The fraction of flat spectrum sources in the 8.5 GHz selected sample is 0.60. Table 5 gives individual spectral indices or limits (where meaningful limits are available) for both the 1.4 and 8.5 GHz samples.

6.1. The Nature of Flat Spectrum Sources: AGN vs. Starbursts

It has been noted by previous authors that below a few milljansky, the median spectral index for high frequency selected samples ($\nu \geq 5$ GHz) flattens from a value of 0.7 to about 0.3-0.4 and then remains constant for at least two decades in flux density (Windhorst et al. 1993 and references therein). Our spectral index study confirms this trend.

This raises the question of what physical mechanism is responsible for the flattening of the high frequency selected microjansky population. One clue comes from the optical identification of the sources. Of the 26 flat spectrum sources presented here, only 4 can be reliably associated with elliptical galaxies, the majority (70%) residing in mergers, interacting disk systems, or isolated field spirals (Paper I, Richards et al. 1998). Thus the flattening of the spectral index distribution for the microjansky population is unlikely to be due to radio evolution of the elliptical population.

If the 8.5 GHz sample preferentially selects out self-absorbed AGN cores from the microjansky population, then we might expect these sources to have a smaller angular size on average as compared to a 1.4 GHz selected sample. The mean angular size for the 26 flat ($\alpha < 0.5$) spectrum sources of Table 5, is $\theta = 1.7 \pm 0.6$, as compared to $\theta = 1.8 \pm 0.5$, for the 47 steep ($\alpha \geq 0.5$) spectrum sources. Thus there is no evidence for a significant change in source size between the flat and steep spectrum population. Interestingly, there are only four inverted spectrum sources among the flat spectrum sample, indicating that strongly self-absorbed systems are rare among the microjansky population.

In Paper I we considered two possibilities for the origin of microjansky radio emission in distant disk galaxies, 1) increased radio activity associated with a central engine (e.g., Seyfert and LINER AGN), and 2) radio emission excited by star-formation. Both are capable of producing flat radio spectra through synchrotron self-absorption in the case of the former, and through increasing amounts of thermal radio emission in the later. These

two different physical mechanisms take place on very different physical scales. For the case of star formation these scales correspond from approximately 0.1-10 kpc as observed in the local starburst population (Condon 1989). Thus the cosmological microjansky population at a mean redshift of 0.8 (Paper I) should have an angular extent of 0.01-1'' if star formation is the ultimate source of energy powering the radio emission. On the other hand if the radio emission has its origin in an AGN then the flattening of the spectral index distribution can be attributed to partial self-absorption. In this case the observed flux density of the source makes calculation of a minimum angular size for synchrotron self-absorption possible (Pacholczyk 1970). For a 100 μ Jy source with a critical absorption frequency of 1.4 GHz and an assumed magnetic field strength no larger than 10^{-4} Gauss, the characteristic angular size scale is of order 10^{-5} arcsec.

Because the radio spectral index is such a sensitive function of absorption varying from -2.5 in the case of pure synchrotron self-absorption, to 0.8 for a standard transparent, non thermal spectrum, the observation of low dispersion in the flat spectral indices of the microjansky population (i.e., very few inverted spectrum sources) would suggest that we are seeing very nearly the same fraction of absorbed radiation in all sources. Perhaps a more natural explanation for the observed spectral index distribution of flat spectrum microjansky radio sources is that we are observing varying ratios of thermal to synchrotron emission causing the spectral indices to vary from -0.1 to 0.8 (cf., Condon 1992). This could be due to the combined effect of a radio K-correction which serves to bring a greater fraction of bremsstrahlung radiation into the observed radio window for sources at appreciable redshifts, as well as a steepening of the synchrotron radiation itself as a result of synchrotron and Compton losses off the microwave background. A flattening of the relativistic electron energy spectrum could flatten the observed synchrotron spectral index as well. Sub-arcsecond radio observations of the microjansky population are necessary to discriminate between these possibilities (Muxlow et al. 1998). High frequency observations

would also be useful to determine the slope of the radio spectrum in these distant radio sources, but will not be feasible until the commissioning of the Millimeter Array or until the expansion of the high frequency capabilities of the VLA.

7. Conclusions

We have presented a complete catalog of 371 radio sources brighter than $40 \mu\text{Jy}$ at 1.4 GHz in a 0.3 deg^2 field centered on the Hubble Deep Field. This is the most sensitive survey available at this resolution ($2''$) and frequency. For a subsample of these sources we have calculated two point spectral indices based on 8.5 GHz mosaic observations.

The principal results of this study are:

1. We have extended the direct source count at 1.4 GHz to $40 \mu\text{Jy}$, confirming that the differential slope for radio sources remains steep at $\gamma = -2.4$ to this level.
2. The average angular size for the microjansky population is observed to decrease as a function of flux density. The mean size for radio sources between $40\text{-}1000 \mu\text{Jy}$ is $2.0''$, consistent with their association with large disk galaxies at $z \sim 1$.
3. Microjansky radio sources appear to be clustered on scales of $1'\text{-}40'$, corresponding to projected distances of $0.5\text{-}20 \text{ Mpc}$.
4. The average spectral index for a 1.4 GHz selected subsample is $\bar{\alpha}_{1.4} = 0.85 \pm 0.2$, indicating optically thin synchrotron emission as the dominant radio emission mechanism. For a 8.5 GHz selected sample, the mean is $\bar{\alpha}_{8.5} = 0.4 \pm 0.1$. This flattening of the spectral index distribution over that of samples selected above a few millijansky is consistent with either the cosmological evolution of the disk galaxy AGN population (LINERs and Seyferts) or of their star-formation activity. We suggest that we are observing increasing amounts

of bremsstrahlung radiation in these sources, causing the observed decrease in the spectral index distribution at 8.5 GHz.

I thank my collaborators Ed Fomalont, Ken Kellermann, Bruce Partridge, Rogier Windhorst, and Tom Muxlow for their help with this project. This study would not have been possible without the expert assistance of the NRAO staff in the planning, execution, and analysis of these observations, especially F. Owen and M. Rupen. This work benefited from suggestions by J. Condon and J. Wall. I also thank L. Cowie and A. Barger for pointing out a positional inconsistency in an earlier version of this work.

8. References

- Cillegi, P. et al. 1998, MNRAS, in press
- Clark, B. G. 1980, A& A, 89, 377
- Coleman, P. H. & Condon, J. J. 1985, AJ, 90, 1431
- Condon, J. J. 1989, ApJ, 338, 13
- Condon, J. J. 1992, ARA & A, 30, 575
- Condon, J. J. 1997, PASP, 109, 166
- Cornwell, T. J. & Perley, R. A. 1992, A & A, 261, 353
- Cress, C., Helfand, D., Becker, R., Gregg, M. & White, R. 1996, ApJ, 473, 7
- Donnelly, R. H., Partridge, R. B & Windhorst, R. A. 1987, ApJ, 321, 94
- Feigelson, E. D. & Nelson, P. I. 1985, ApJ, 293, 192
- Fomalont, E. B., Windhorst, R. A., Kristian, J. A. & Kellermann, K. I. 1991, AJ, 102, 1258
- Fomalont, E. B., Goss, W. M., Lyne, A. G., Manchester, R. N. & Justtanont, K. 1992,
MNRAS, 258, 497
- Fomalont, E. B., Kellermann, K. I., Richards, E. A., Windhorst, R. A. & Partridge, R. B.
1997, ApJL, 475, 5
- Gruppioni, C., Zamorani, G., De Rutter, H. R., Parma, P, Mignoli, M. & Hasinger, G
1997, MNRAS, 286, 470
- Hammer, F., Crampton, D., Lilly, S. J., LeFevre, O. & Kenet, T. 1995, MNRAS, 276, 1085
- Hopkins, A., Afonso, J., Cram, L. & Mobasher, B. 1999, ApJL, in press

- Hopkins, A. M., Mobasher, B., Cram, L. & Rowan-Robinson, M. 1998, MNRAS, 296, 839
- Isobe, T. & Feigelson, E. D. 1991, ASURV, Rev. 1.2
- Katgert, P., Oort, J. & Windhorst, R. 1988, A& A, 195, 21
- Ling, E. N., Frenk, C. S. & Barrow, J. D. 1986, MNRAS, 223, 21p
- Magliocchetti, M., Maddox, S., Lahav, O. & Wall, J. 1998, MNRAS, 300, 257
- Mitchell, K. J. & Condon, J. J. 1985, AJ, 90, 1987
- Muxlow et al. 1999, *in preparation*
- Oort, J. A. 1987, A & AS, 71, 2210
- Oort, J. A. 1988, A & A, 193, 50
- Oort, J. A. & Windhorst, R. A. 1985, A&A, 145, 4050
- Pacholczyk 1970, Radio Astrophysics (San Francisco: W. H. Freeman)
- Peebles, P. J. E. 1980, The Large Scale Structure of the Universe (Princeton: Princeton University Press)
- Richards, E. A. 1996, in IAU 175: Extragalactic Radio Sources, eds., Ekers, R., Fanti, C. & Padrielli, L., 593
- Richards, E. A., Kellermann, K. I., Fomalont, E. B., Windhorst, R. A., & Partridge, R. B. 1998a, AJ, 116, 1039 (Paper I)
- Richards, E. A. 1999b, et al., *in preparation* (Paper III)
- Rowan-Robinson, M. *et al.* 1997, MNRAS, 289, 490
- Windhorst, R. A., Fomalont, E. B., Kellermann, K. I., Partridge, R. B., Richards, E. A., Franklin, B. E., Pascarella, S. M. & Griffiths, R. E. 1995, Nature, 375, 471

Windhorst, R. A., Fomalont, E. B., Partridge, R. B. & Lowenthal, J. D. 1993, ApJ, 405, 498

Windhorst, R. A., van Heerde, G. M. & Katgert, P. 1984, A & AS, 58, 1

9. Figure Captions

1. A greyscale of the inner $9.5' \times 9.5'$ of the 1.4 GHz image. The pixel range is from $-10 - 20 \mu\text{Jy}$. The effective resolution is $1.8''$ with an rms noise of $7.5 \mu\text{Jy}$. The image has been corrected by the primary beam attenuation.

2. Here we show the same $9.5' \times 9.5'$ area at 8.5 GHz. The greyscale extends from $-2 - 6 \mu\text{Jy}$. The effective resolution is $3.5''$ with an rms noise of $1.6 \mu\text{Jy}$. This image has been corrected by the primary beam attenuation and hence the noise is not uniform.

3. The total off-axis response of a point source due to the combined effects of bandwidth smearing, time averaging smearing, and the primary beam correction (gain). The relative amplitude decrease due to time average smearing (tsmear), bandwidth smearing (bwsmeas), and the primary beam attenuation (pbcor) are also shown.

4. The angular size distribution for the 1.4 GHz complete sample. Notice the increasing number of upper limits at lower flux density levels.

5. The 1.4 GHz median angular size vs. flux density relation for microjansky radio sources. Points from Oort (1988; O88), Coleman & Condon (1985; CC), and this study are plotted. The curve shown has been calculated according to the model given in §4. The broken line represents a median angular size independent of flux density.

6a. The 1.4 GHz source counts from this field and other deep radio surveys are shown. The count is presented in differential form normalized to the counts expected in a Euclidean geometry. For comparison, counts from Mitchell & Condon (1985; MC), the Phoenix Deep Field (Hopkins et al. 1998; PDF), Oort & Windhorst (1985, OW85), and the ELAIS survey (Cillegi et al. 1998; ELAIS) are plotted. The best fit to the earlier deep survey compilation by Katgert et al. (1988) is shown as a solid line.

6b. A blow-up of the sub-millijansky counts. The solid line is the best fit to the

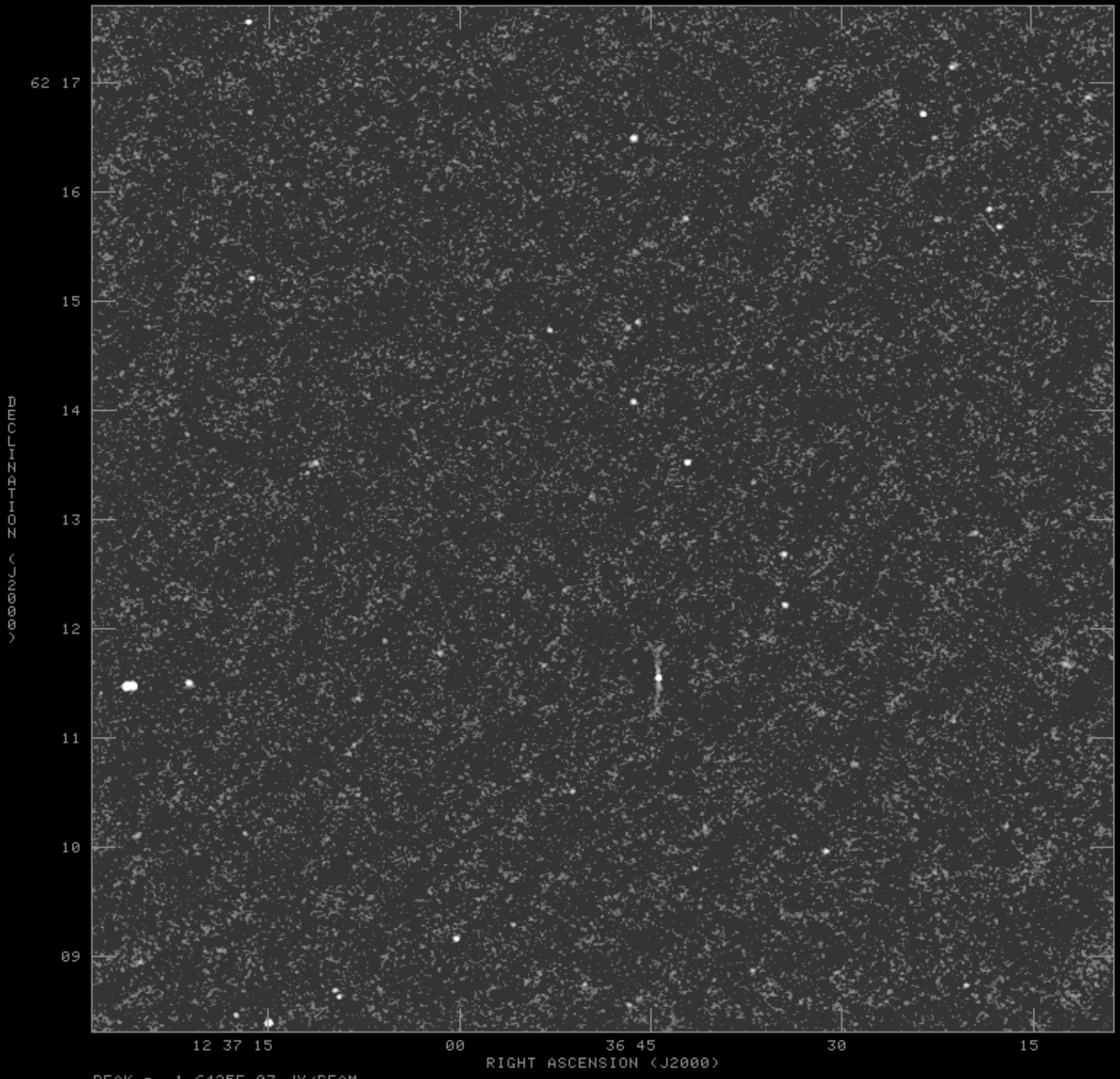
current survey data. There is good evidence for field to field fluctuations above that of the statistical noise.

7. The correlation function of the HDF radio survey is shown as heavy dots. The correlation function in the Lynx3 survey of Oort (1987) is shown for comparison.

8. The spectral index flux density distribution for the 1.4 GHz selected sample. The mean of the sample as calculated by survival analysis is shown as the broken line.

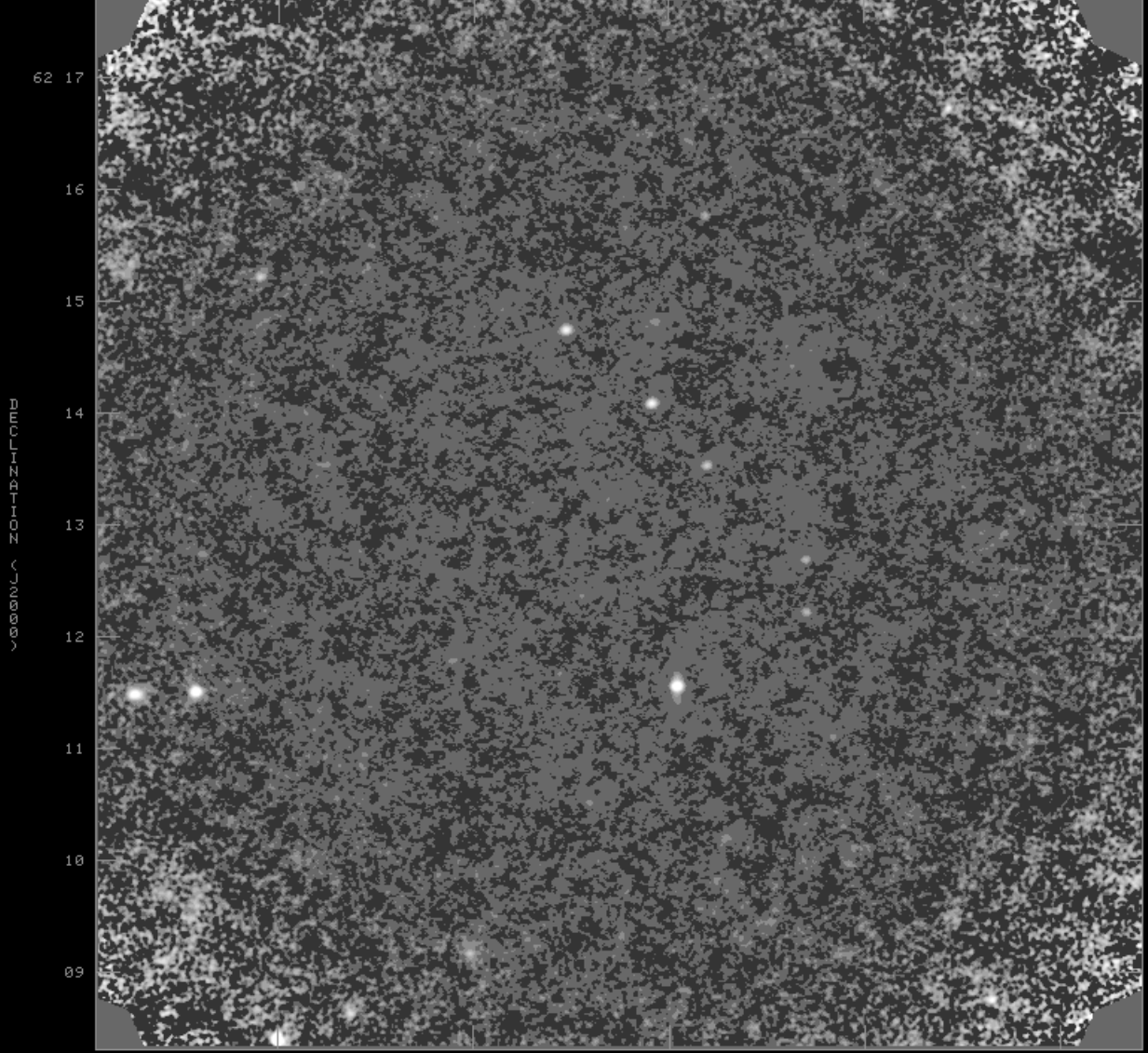
9. The spectral index flux density distribution for the 8.5 GHz selected sample. The mean of the sample as calculated by survival analysis is shown as the broken line.

HDF IPOL 1400.050 MHZ



PEAK = 1.6425E-03 JY/BEAM
IMNAME= HDF.RSTOR.2

HDF E IPOL 8460.100 MHZ



PEAK = 1.0845E-03 JY/BEAM
IMNAME= XMOS.HGEOM.2

RIGHT ASCENSION (J2000)

Table 2: Complete 1.4 GHz Source List

Right Ascension <i>hh mm ss</i>	Declination ° ' "	θ (")	σ_{snr}	$S_{1.4}$ (μ Jy)		
12 33 36.583	0.015 62 30 19.72	0.10	6.5	48.7	50900.0	2560.0
12 34 00.107	0.027 62 12 22.16	0.19	–	5.7	260.0	28.3
12 34 03.519	0.017 62 14 20.75	0.12	<2.1	15.5	693.0	42.2
12 34 10.657	0.019 62 06 15.96	0.13	3.1	10.7	629.0	40.2
12 34 11.242	0.015 62 16 16.78	0.11	11.7	27.3	9700.0	487.0
12 34 14.339	0.028 62 21 09.18	0.19	–	5.4	253.0	36.2
12 34 16.118	0.021 62 07 22.75	0.15	3.1	8.1	453.0	31.7
12 34 23.970	0.022 62 20 38.23	0.16	3.9	7.5	394.0	29.2
12 34 26.705	0.015 62 13 31.90	0.11	3.2	24.9	1350.0	69.9
12 34 26.855	0.015 62 14 54.63	0.10	<2.0	45.1	2710.0	140.0
12 34 28.656	0.027 62 18 27.80	0.19	–	5.6	180.0	26.3
12 34 29.878	0.015 62 18 06.62	0.10	3.0	29.6	1350.0	69.8
12 34 31.903	0.024 62 19 50.98	0.16	–	6.9	235.0	22.1
12 34 34.706	0.023 62 20 22.98	0.16	–	7.2	224.0	21.7
12 34 35.807	0.023 62 24 39.63	0.16	–	7.3	320.0	35.9
12 34 51.106	0.022 62 07 58.16	0.15	–	7.6	165.0	16.4
12 34 51.464	0.021 62 05 48.28	0.15	–	8.6	204.0	18.4
12 34 51.724	0.027 61 58 50.06	0.19	–	5.6	269.0	28.2
12 34 52.278	0.014 62 02 35.70	0.10	15.2	2500	293000.0	14600.0
12 34 56.990	0.023 62 25 27.00	0.16	–	7.3	172.0	22.0
12 35 00.128	0.018 62 11 01.00	0.13	<2.1	12.0	211.0	16.1
12 35 05.666	0.023 62 16 32.28	0.16	–	6.9	115.0	13.2
12 35 06.051	0.018 62 27 56.25	0.13	3.3	11.6	730.0	43.3
12 35 06.555	0.026 62 07 07.92	0.18	–	6.0	106.0	13.7
12 35 06.785	0.023 62 16 39.55	0.16	–	7.1	116.0	13.2
12 35 09.078	0.025 62 10 55.29	0.17	–	6.3	96.6	12.3
12 35 09.137	0.024 62 17 33.60	0.17	–	6.8	94.6	12.8
12 35 09.611	0.017 62 08 55.80	0.12	3.0	12.9	307.0	19.3
12 35 09.918	0.026 62 20 56.13	0.18	–	6.1	117.0	14.6
12 35 10.276	0.015 62 22 01.80	0.10	<2.0	42.8	1880.0	98.6
12 35 10.651	0.015 62 19 37.24	0.11	<2.0	28.1	493.0	27.8
12 35 13.145	0.024 62 08 02.82	0.17	–	6.7	105.0	12.7
12 35 13.589	0.022 62 12 40.10	0.16	–	7.5	111.0	12.1
12 35 13.729	0.017 62 09 18.63	0.12	<2.1	14.5	215.0	15.5
12 35 14.590	0.023 62 17 36.62	0.16	–	7.0	106.0	12.5
12 35 14.937	0.016 62 15 09.85	0.11	<2.0	18.7	266.0	17.2

12 35 15.165	0.020	62 10 13.41	0.14	–	9.0	128.0	12.6
12 35 16.197	0.015	62 16 36.30	0.10	<2.0	39.2	563.0	30.3
12 35 18.667	0.023	62 18 54.94	0.16	–	7.4	113.0	12.8
12 35 19.398	0.021	62 20 24.98	0.15	–	8.2	137.0	13.9
12 35 21.190	0.021	61 59 26.19	0.14	3.4	8.6	378.0	25.9
12 35 21.622	0.014	62 18 07.07	0.10	<1.9	64.9	2100.0	108.0
12 35 21.651	0.019	62 07 20.21	0.14	<2.2	9.8	143.0	13.2
12 35 21.850	0.020	62 12 24.31	0.14	–	8.8	116.0	11.7
12 35 22.229	0.020	62 09 53.55	0.14	–	8.9	117.0	11.9
12 35 22.601	0.015	62 22 47.91	0.10	<2.0	40.4	1630.0	86.1
12 35 23.743	0.023	62 16 48.54	0.16	–	7.2	95.3	11.5
12 35 27.444	0.017	62 19 37.58	0.12	<2.1	13.3	193.0	14.7
12 35 29.358	0.018	62 12 56.44	0.13	<2.1	11.1	135.0	11.8
12 35 31.076	0.025	62 13 43.66	0.17	–	6.3	74.5	10.2
12 35 31.558	0.027	62 11 17.30	0.19	–	5.7	66.1	10.1
12 35 31.749	0.020	62 24 52.44	0.14	<2.2	9.6	207.0	17.8
12 35 32.537	0.021	61 55 17.82	0.15	–	8.0	358.0	30.8
12 35 35.036	0.023	62 08 50.55	0.16	–	7.0	82.3	10.6
12 35 37.407	0.024	62 10 03.13	0.17	–	6.6	73.5	10.1
12 35 37.438	0.021	62 05 37.23	0.15	–	8.0	110.0	12.0
12 35 38.032	0.014	62 19 32.26	0.10	5.9	100.7	6340.0	318.0
12 35 38.104	0.020	62 22 40.96	0.14	–	9.1	149.0	14.2
12 35 38.267	0.028	62 06 51.46	0.19	–	5.5	68.9	10.7
12 35 38.515	0.014	62 16 43.07	0.10	19.7	78.7	3550.0	179.0
12 35 39.909	0.023	62 14 30.66	0.16	–	7.0	74.9	9.8
12 35 39.953	0.023	62 14 41.98	0.16	–	7.1	76.2	9.9
12 35 40.388	0.028	62 16 23.80	0.19	–	5.4	60.1	9.8
12 35 40.998	0.022	62 18 28.20	0.16	–	7.5	89.0	10.8
12 35 41.100	0.029	62 01 20.42	0.20	–	5.4	111.0	14.5
12 35 41.109	0.021	62 08 21.46	0.15	3.9	8.2	270.0	16.5
12 35 42.083	0.022	62 05 35.75	0.16	–	7.6	100.0	11.6
12 35 44.177	0.021	61 57 31.29	0.15	3.6	8.0	526.0	32.0
12 35 44.782	0.019	62 22 42.06	0.13	6.6	10.0	442.0	24.9
12 35 45.056	0.022	61 54 48.65	0.15	–	7.7	620.0	39.5
12 35 45.737	0.016	62 02 40.18	0.11	2.4	15.9	318.0	19.9
12 35 47.105	0.023	62 20 09.50	0.16	–	7.4	92.5	11.1

12 35 47.760	0.019	62 10 57.81	0.13	<2.2	9.9	99.8	10.1
12 35 47.962	0.018	62 15 29.42	0.13	<2.1	11.7	118.0	10.6
12 35 48.101	0.022	62 10 34.97	0.15	–	8.0	80.2	9.7
12 35 48.814	0.022	62 26 02.24	0.15	–	7.7	130.0	15.7
12 35 49.422	0.022	62 15 36.77	0.16	–	7.5	74.6	9.5
12 35 50.618	0.014	62 27 58.03	0.10	4.4	116.7	11400.0	570.0
12 35 50.716	0.019	62 07 21.52	0.13	<2.2	10.4	115.0	11.0
12 35 50.927	0.019	62 14 57.42	0.13	<2.1	10.9	107.0	10.2
12 35 51.239	0.017	62 25 14.79	0.12	2.4	15.5	354.0	22.2
12 35 51.943	0.020	62 08 09.09	0.14	<2.2	9.4	98.7	10.3
12 35 53.281	0.026	62 13 37.85	0.18	–	6.1	58.4	9.0
12 35 53.748	0.024	62 21 55.20	0.17	–	6.8	83.6	11.5
12 35 54.092	0.027	62 10 43.37	0.19	–	5.6	53.7	9.0
12 35 55.144	0.016	62 09 01.80	0.11	<2.0	21.3	212.0	13.7
12 35 55.977	0.023	62 15 55.78	0.16	2.5	7.3	89.7	9.7
12 35 56.380	0.026	62 02 47.23	0.18	–	5.9	87.7	12.1
12 35 57.023	0.028	62 02 12.23	0.19	–	5.5	98.7	12.6
12 35 57.624	0.028	62 08 08.11	0.19	–	5.4	68.6	9.5
12 35 57.953	0.015	62 15 36.86	0.11	<2.0	22.2	209.0	13.4
12 35 59.752	0.017	62 15 50.05	0.12	2.7	14.7	212.0	13.5
12 36 00.064	0.019	62 02 53.36	0.13	2.8	9.9	262.0	17.1
12 36 00.164	0.017	62 10 47.38	0.12	<2.1	14.3	131.0	10.6
12 36 00.940	0.024	62 18 07.21	0.17	–	6.5	65.7	9.4
12 36 01.576	0.026	62 28 19.54	0.19	–	5.8	204.0	19.4
12 36 01.796	0.019	62 11 26.42	0.13	<2.2	10.3	93.2	9.5
12 36 01.987	0.027	62 06 04.93	0.19	–	5.7	77.2	10.1
12 36 02.339	0.025	62 24 25.73	0.18	–	6.3	102.0	13.0
12 36 03.276	0.017	62 11 11.17	0.12	<2.1	13.8	124.0	10.3
12 36 04.196	0.021	62 16 20.34	0.14	–	8.7	80.6	9.3
12 36 04.289	0.027	62 08 11.57	0.19	–	5.7	55.4	9.1
12 36 05.503	0.029	62 01 58.79	0.20	–	5.4	90.3	12.3
12 36 06.484	0.023	62 06 08.78	0.16	–	7.1	76.1	9.9
12 36 06.622	0.016	62 09 51.33	0.11	2.2	19.4	196.0	12.8
12 36 06.887	0.021	62 10 21.67	0.15	–	8.4	74.4	9.0
12 36 07.139	0.026	62 13 28.77	0.18	–	5.8	51.3	8.4
12 36 08.137	0.015	62 10 36.01	0.11	<2.0	24.7	217.0	13.6

12 36 08.234	0.022	62 15 52.92	0.15	–	6.6	59.3	8.6
12 36 08.582	0.022	62 14 35.20	0.16	–	7.5	68.9	8.8
12 36 08.734	0.020	62 30 54.30	0.14	<2.2	9.6	419.0	29.8
12 36 09.430	0.025	62 20 42.60	0.18	–	6.1	68.7	10.0
12 36 09.901	0.020	62 20 45.97	0.14	–	8.9	100.0	10.7
12 36 10.187	0.027	62 06 44.90	0.19	–	5.5	55.6	9.3
12 36 10.526	0.025	62 08 11.08	0.17	–	6.3	59.0	9.0
12 36 10.583	0.018	62 16 51.77	0.12	2.7	12.4	139.0	10.8
12 36 10.708	0.018	62 23 45.24	0.13	<2.1	11.9	173.0	14.1
12 36 11.103	0.018	62 22 28.69	0.13	<2.1	11.9	154.0	12.8
12 36 11.408	0.020	62 21 49.93	0.14	–	9.1	111.0	11.4
12 36 12.223	0.017	62 04 48.70	0.12	<2.1	14.1	161.0	12.5
12 36 12.455	0.020	62 11 40.46	0.14	3.9	9.7	174.0	11.8
12 36 13.618	0.022	62 02 48.56	0.16	–	7.4	100.0	11.7
12 36 14.762	0.028	62 01 34.00	0.19	–	5.4	82.4	12.1
12 36 14.805	0.022	61 54 29.90	0.16	–	7.5	285.0	26.3
12 36 15.035	0.023	62 06 13.21	0.16	–	7.0	89.2	10.0
12 36 15.607	0.025	62 09 46.74	0.18	–	5.6	48.8	8.3
12 36 16.091	0.027	62 22 03.96	0.19	–	5.6	68.4	10.5
12 36 16.135	0.025	62 15 13.98	0.17	–	6.4	53.9	8.4
12 36 16.524	0.026	62 07 02.71	0.18	–	5.9	56.6	9.1
12 36 17.105	0.023	62 10 11.57	0.16	–	7.3	62.0	8.6
12 36 17.565	0.015	62 15 40.91	0.11	<2.0	23.6	200.0	12.8
12 36 18.037	0.028	62 16 35.69	0.19	–	5.4	47.1	8.4
12 36 18.348	0.016	62 15 50.67	0.11	<2.0	17.8	151.0	11.0
12 36 19.290	0.021	62 05 58.94	0.15	–	8.5	86.7	9.9
12 36 19.508	0.020	62 12 52.70	0.14	2.7	9.4	108.0	9.4
12 36 20.285	0.017	62 08 44.27	0.12	<2.1	14.0	123.0	10.2
12 36 20.781	0.024	62 25 09.76	0.17	–	6.7	111.0	13.1
12 36 21.025	0.022	62 07 13.22	0.15	–	7.6	90.4	9.6
12 36 21.098	0.018	62 21 33.88	0.12	<2.1	12.5	143.0	11.9
12 36 21.267	0.025	62 11 09.51	0.17	–	6.3	52.6	8.2
12 36 21.271	0.016	62 17 08.69	0.11	<2.0	17.0	148.0	11.0
12 36 22.408	0.023	62 15 44.75	0.16	2.9	7.0	83.9	8.9
12 36 22.514	0.016	62 06 54.04	0.11	<2.0	16.6	159.0	11.7
12 36 22.656	0.021	62 16 29.94	0.15	–	8.3	70.9	8.7

12 36 22.718	0.023	62 09 45.81	0.16	—	6.1	51.0	8.2
12 36 23.350	0.023	62 06 05.29	0.16	—	7.2	71.7	9.5
12 36 23.406	0.025	62 03 34.28	0.17	—	6.3	76.8	10.6
12 36 23.550	0.014	62 16 42.90	0.10	<1.9	56.3	481.0	25.4
12 36 23.914	0.025	62 03 30.81	0.18	—	6.1	75.1	10.6
12 36 24.267	0.024	62 10 17.33	0.17	—	6.5	54.2	8.3
12 36 24.298	0.024	62 24 20.82	0.17	—	6.8	87.9	12.0
12 36 24.756	0.020	62 17 43.88	0.14	—	8.9	78.8	9.1
12 36 28.906	0.026	62 06 16.00	0.18	—	6.0	58.1	9.1
12 36 29.019	0.022	62 10 46.03	0.15	—	7.8	81.4	8.7
12 36 29.245	0.016	62 02 53.94	0.11	<2.0	16.9	216.0	14.8
12 36 29.968	0.021	62 05 42.21	0.15	—	8.2	82.9	9.7
12 36 30.094	0.026	62 09 23.59	0.18	—	5.6	46.3	8.2
12 36 30.463	0.025	62 08 51.03	0.18	—	5.7	48.0	8.2
12 36 31.197	0.015	62 28 05.98	0.11	3.6	23.1	1230.0	63.4
12 36 31.252	0.017	62 09 57.99	0.12	2.5	15.3	152.0	10.9
12 36 32.356	0.020	62 17 00.06	0.14	—	8.8	81.8	8.9
12 36 32.579	0.023	62 08 00.22	0.16	2.6	7.3	90.6	9.3
12 36 32.796	0.020	62 24 20.34	0.14	<2.2	9.4	139.0	13.0
12 36 33.531	0.016	62 21 45.02	0.11	<2.0	20.3	230.0	14.9
12 36 33.666	0.021	62 04 45.37	0.14	—	8.7	93.6	10.3
12 36 33.746	0.027	62 10 06.23	0.19	—	5.7	46.5	8.1
12 36 34.197	0.023	62 20 40.70	0.16	—	7.0	72.6	9.6
12 36 34.454	0.028	61 55 34.37	0.19	—	5.4	167.0	20.4
12 36 34.464	0.015	62 12 13.33	0.11	2.3	23.5	233.0	13.9
12 36 34.530	0.016	62 12 41.23	0.11	2.5	20.8	230.0	13.8
12 36 34.635	0.019	62 19 26.33	0.13	<2.2	10.4	98.8	9.8
12 36 34.888	0.023	62 19 23.69	0.16	—	7.2	68.3	9.1
12 36 35.618	0.022	62 14 24.33	0.16	2.8	7.5	87.8	8.8
12 36 36.335	0.027	62 07 06.81	0.19	—	5.4	49.9	8.5
12 36 36.926	0.022	62 13 20.36	0.15	—	6.6	50.0	7.9
12 36 37.041	0.021	62 08 52.58	0.15	—	8.4	71.1	8.7
12 36 38.985	0.020	62 02 30.77	0.14	2.5	9.0	166.0	13.2
12 36 40.151	0.014	62 20 37.38	0.10	<1.9	91.3	1840.0	93.8
12 36 40.567	0.015	62 18 33.17	0.10	<2.0	35.9	324.0	18.2
12 36 40.728	0.026	62 10 10.85	0.18	3.7	5.9	86.8	8.8

12 36 41.554	0.020	62 09 48.63	0.14	–	9.1	75.8	8.6
12 36 42.109	0.015	62 13 31.73	0.10	2.2	51.2	467.0	24.6
12 36 42.161	0.028	62 24 38.89	0.20	–	5.4	82.1	11.8
12 36 42.229	0.017	62 15 45.73	0.12	2.4	14.5	150.0	10.7
12 36 43.642	0.018	62 25 11.73	0.12	<2.1	12.3	202.0	15.4
12 36 43.847	0.029	62 05 59.53	0.20	–	5.4	62.5	9.2
12 36 44.369	0.014	62 11 33.19	0.10	12.0	55.2	1290.0	61.2
12 36 44.503	0.020	62 01 20.80	0.14	–	9.3	143.0	13.2
12 36 45.864	0.027	62 07 54.45	0.19	–	5.5	48.9	8.4
12 36 46.047	0.017	62 14 48.85	0.12	2.3	12.9	124.0	9.8
12 36 46.337	0.015	62 16 29.77	0.10	2.7	28.5	393.0	21.1
12 36 46.362	0.016	62 14 04.98	0.11	<2.0	21.1	179.0	11.7
12 36 46.710	0.020	62 08 33.62	0.14	–	9.2	80.1	8.9
12 36 46.736	0.027	62 12 26.93	0.19	–	5.5	72.0	9.1
12 36 46.755	0.024	62 14 45.88	0.16	3.1	6.9	117.0	9.6
12 36 48.461	0.025	62 24 24.92	0.18	–	6.1	92.4	11.8
12 36 49.001	0.015	62 04 38.80	0.10	<2.0	36.0	850.0	46.3
12 36 49.165	0.017	61 59 30.90	0.12	<2.1	13.3	264.0	18.4
12 36 49.499	0.018	62 21 43.18	0.12	<2.1	12.0	138.0	11.6
12 36 49.656	0.027	62 13 13.16	0.19	–	5.6	49.2	7.9
12 36 49.663	0.015	62 07 38.18	0.10	<2.0	33.8	307.0	17.4
12 36 50.047	0.026	62 08 01.91	0.18	–	6.0	53.8	8.5
12 36 50.205	0.020	62 08 44.72	0.14	–	8.8	76.4	8.8
12 36 50.208	0.019	62 27 32.37	0.13	4.4	10.5	660.0	35.8
12 36 51.052	0.026	62 05 29.32	0.18	–	5.9	60.3	9.3
12 36 51.148	0.018	62 10 30.95	0.13	<2.1	11.3	95.0	9.0
12 36 51.498	0.023	62 06 44.03	0.16	–	7.2	68.5	9.0
12 36 51.701	0.028	62 05 02.68	0.19	–	5.4	57.6	9.4
12 36 51.797	0.027	62 12 21.42	0.19	–	5.7	49.3	7.9
12 36 52.354	0.026	62 02 06.30	0.18	–	6.1	85.2	11.3
12 36 52.814	0.021	62 18 07.40	0.15	3.7	8.1	350.0	23.8
12 36 52.955	0.016	62 14 44.34	0.11	2.5	15.9	168.0	11.3
12 36 53.431	0.022	62 11 40.10	0.15	–	7.8	65.7	8.2
12 36 54.303	0.023	62 07 45.62	0.16	–	7.1	63.2	8.7
12 36 54.708	0.023	62 10 39.57	0.16	–	6.2	48.2	8.0
12 36 54.786	0.028	62 04 26.87	0.19	–	5.5	60.5	9.7

12 36 54.859	0.024	62 05 35.22	0.17	2.7	6.8	110.0	10.3
12 36 55.768	0.025	61 56 48.08	0.17	3.6	6.4	312.0	22.5
12 36 55.785	0.022	62 09 17.66	0.15	–	7.6	64.2	8.4
12 36 55.837	0.014	61 56 59.39	0.10	37.2	83.3	36900.0	1850.0
12 36 55.946	0.018	62 08 08.43	0.12	<2.1	12.1	106.0	9.6
12 36 56.126	0.025	61 56 44.46	0.18	5.0	6.1	552.0	32.1
12 36 56.174	0.028	62 26 31.39	0.20	–	5.4	106.0	13.8
12 36 56.505	0.027	62 19 38.07	0.19	–	5.5	53.3	8.9
12 36 56.605	0.027	62 12 07.58	0.19	–	5.5	46.2	7.9
12 36 56.884	0.027	62 13 02.52	0.19	–	5.7	49.5	7.9
12 36 57.858	0.024	62 23 32.53	0.17	–	6.6	89.2	11.2
12 36 59.356	0.015	62 18 32.58	0.10	<2.0	29.8	506.0	30.2
12 36 59.617	0.029	62 25 09.94	0.20	–	5.5	90.3	12.4
12 36 59.948	0.023	62 14 49.87	0.16	–	6.1	47.0	7.9
12 37 00.263	0.015	62 09 09.99	0.10	<2.0	38.5	324.0	18.0
12 37 01.104	0.015	62 21 09.68	0.10	<2.0	28.3	304.0	17.7
12 37 01.548	0.025	62 20 25.07	0.18	–	6.3	63.5	9.4
12 37 01.560	0.020	62 11 46.86	0.14	3.0	9.7	128.0	9.9
12 37 02.123	0.029	62 23 30.56	0.20	–	5.5	78.7	11.1
12 37 02.672	0.027	62 30 45.38	0.19	–	5.5	188.0	21.6
12 37 02.762	0.026	62 14 01.61	0.18	–	5.4	41.4	7.8
12 37 04.077	0.025	62 07 55.54	0.17	–	5.8	50.7	8.4
12 37 05.211	0.024	62 19 50.89	0.17	–	6.7	65.9	9.2
12 37 05.875	0.025	62 11 53.66	0.17	–	6.4	52.5	8.0
12 37 06.769	0.021	62 07 22.42	0.15	–	8.0	72.8	9.0
12 37 06.893	0.019	62 23 06.53	0.13	2.5	10.5	189.0	13.9
12 37 07.203	0.027	62 14 08.33	0.19	–	5.5	45.3	7.9
12 37 07.521	0.025	62 21 48.24	0.18	–	6.1	70.0	10.1
12 37 07.925	0.019	62 05 45.21	0.14	<2.2	9.8	98.0	10.1
12 37 07.959	0.023	62 11 21.81	0.16	–	7.4	60.3	8.2
12 37 08.114	0.026	62 16 59.30	0.18	–	5.9	50.4	8.3
12 37 08.335	0.027	62 10 56.23	0.19	–	5.5	45.1	8.0
12 37 08.786	0.017	62 22 01.91	0.12	<2.1	14.6	170.0	12.8
12 37 09.056	0.021	62 23 19.20	0.14	–	8.6	114.0	11.8
12 37 09.449	0.021	62 08 37.83	0.15	–	8.4	72.0	8.8
12 37 09.769	0.020	62 08 41.22	0.14	–	7.9	67.9	8.3

12 37 09.941	0.014	62 22 58.87	0.10	<1.9	55.5	708.0	36.9
12 37 10.018	0.021	62 26 50.25	0.15	5.9	8.1	551.0	30.6
12 37 11.339	0.019	62 13 31.26	0.13	<2.1	10.8	132.0	10.1
12 37 11.946	0.025	62 13 25.89	0.17	–	6.5	53.9	8.1
12 37 12.530	0.024	61 57 06.75	0.16	3.4	6.9	368.0	24.4
12 37 12.555	0.024	62 24 25.02	0.17	–	6.7	100.0	12.2
12 37 13.582	0.029	62 16 04.00	0.20	–	5.5	55.3	8.3
12 37 13.870	0.014	62 18 26.47	0.10	<1.9	64.9	595.0	30.9
12 37 14.336	0.028	62 05 04.15	0.19	–	5.5	58.6	9.6
12 37 14.964	0.014	62 08 23.45	0.10	<1.9	79.3	1380.0	70.8
12 37 15.618	0.027	62 01 08.51	0.19	3.4	5.7	145.0	13.6
12 37 16.032	0.020	62 03 23.04	0.14	–	8.8	109.0	11.4
12 37 16.380	0.015	62 15 12.61	0.11	<2.0	22.5	187.0	12.2
12 37 16.530	0.025	62 02 10.06	0.18	–	6.1	85.2	11.6
12 37 16.560	0.022	62 16 43.94	0.15	–	7.8	66.5	8.7
12 37 16.681	0.015	62 17 33.53	0.10	<2.0	39.0	346.0	19.2
12 37 16.787	0.022	62 10 07.45	0.16	–	7.6	63.3	8.5
12 37 17.511	0.023	62 08 27.43	0.16	2.1	7.1	126.0	17.5
12 37 17.608	0.024	61 56 45.38	0.17	3.0	6.6	311.0	22.9
12 37 18.578	0.025	62 03 36.37	0.18	–	6.3	76.7	10.6
12 37 18.716	0.014	62 03 55.81	0.10	<1.9	282.0	6580.0	330.0
12 37 20.019	0.018	62 07 41.45	0.13	2.2	11.5	202.0	19.6
12 37 21.268	0.016	62 11 30.17	0.11	0.9	20.7	382.0	24.7
12 37 21.393	0.015	62 07 08.47	0.10	<2.0	32.5	310.0	17.7
12 37 21.412	0.026	62 13 46.79	0.18	–	6.0	50.5	8.2
12 37 22.301	0.027	62 27 51.84	0.19	3.5	5.6	258.0	19.8
12 37 23.057	0.022	62 05 39.87	0.16	–	7.4	78.5	9.9
12 37 25.045	0.019	62 08 56.67	0.13	<2.2	10.0	90.0	9.4
12 37 25.294	0.025	62 10 06.51	0.17	3.9	6.4	117.0	10.0
12 37 25.679	0.028	62 19 41.40	0.19	3.4	5.4	122.0	10.8
12 37 25.726	0.014	62 11 28.50	0.10	5.5	98.0	5960.0	298.0
12 37 26.370	0.016	61 58 17.94	0.11	3.6	17.0	883.0	46.6
12 37 26.476	0.020	62 20 26.77	0.14	<2.2	9.4	102.0	10.6
12 37 30.799	0.018	62 12 59.14	0.12	<2.1	12.0	107.0	9.6
12 37 31.141	0.025	62 31 37.19	0.17	2.8	6.4	369.0	29.7
12 37 32.642	0.026	62 10 12.87	0.18	–	5.6	50.6	8.5

12 37 34.274	0.020	62 09 31.86	0.14	2.8	9.7	142.0	11.0
12 37 34.513	0.020	62 17 23.29	0.14	2.7	9.5	131.0	10.8
12 37 35.147	0.023	62 25 59.88	0.16	4.0	7.1	381.0	23.2
12 37 35.403	0.026	62 09 41.49	0.18	–	5.9	54.8	8.8
12 37 35.869	0.029	62 24 02.78	0.20	–	5.5	93.1	12.5
12 37 36.502	0.022	62 06 09.50	0.16	–	7.5	81.9	10.2
12 37 36.586	0.024	61 59 19.13	0.17	3.2	6.5	248.0	18.8
12 37 36.879	0.025	62 14 29.40	0.17	–	6.4	57.8	8.7
12 37 37.111	0.027	62 12 05.40	0.19	3.4	5.7	100.0	9.6
12 37 38.118	0.017	62 08 28.12	0.12	<2.1	13.8	135.0	11.0
12 37 38.221	0.022	62 09 20.46	0.16	–	7.5	71.9	9.3
12 37 39.279	0.026	62 20 59.62	0.18	–	6.0	72.5	10.5
12 37 39.329	0.015	62 05 05.64	0.11	<2.0	25.8	309.0	18.3
12 37 40.823	0.027	62 12 31.23	0.19	3.7	5.5	91.0	9.5
12 37 40.898	0.027	62 04 44.10	0.19	–	5.7	71.0	10.7
12 37 41.028	0.022	62 09 11.01	0.15	–	7.7	74.6	9.4
12 37 41.394	0.016	62 12 51.43	0.11	<2.0	17.3	163.0	11.7
12 37 42.825	0.023	62 15 57.48	0.16	–	7.0	67.1	9.2
12 37 44.672	0.023	62 12 19.00	0.16	–	7.0	67.3	9.1
12 37 44.674	0.023	62 23 06.80	0.16	2.9	7.3	184.0	14.6
12 37 44.751	0.024	62 23 03.87	0.17	–	6.8	102.0	12.4
12 37 45.729	0.024	62 14 56.43	0.17	–	6.6	63.6	9.1
12 37 45.734	0.027	62 04 29.36	0.19	–	5.6	73.7	11.0
12 37 46.641	0.015	62 17 38.46	0.10	<1.9	51.5	998.0	53.2
12 37 47.084	0.020	62 16 31.77	0.14	<2.2	9.6	96.9	10.1
12 37 47.544	0.024	62 22 49.86	0.17	–	6.9	102.0	12.4
12 37 47.940	0.024	62 14 42.20	0.17	–	6.6	64.4	9.2
12 37 50.262	0.020	62 13 59.16	0.14	–	9.1	90.5	9.8
12 37 50.491	0.022	62 11 43.33	0.16	4.5	7.5	198.0	13.2
12 37 51.217	0.016	62 19 19.11	0.11	<2.0	18.8	223.0	14.8
12 37 51.428	0.019	62 22 59.70	0.13	<2.2	10.1	157.0	14.0
12 37 52.699	0.022	62 07 19.40	0.16	–	7.5	86.6	10.5
12 37 52.713	0.025	62 16 27.95	0.18	–	6.1	79.8	9.9
12 37 52.845	0.017	62 21 45.04	0.12	<2.1	13.6	193.0	14.6
12 37 53.347	0.019	62 22 19.79	0.14	2.8	9.7	219.0	15.7
12 37 54.239	0.024	62 13 40.05	0.17	–	6.5	67.0	9.4

12 37 54.340	0.015	62 10 59.51	0.11	<2.0	27.6	285.0	16.8
12 37 55.457	0.025	62 11 42.12	0.17	–	6.4	66.1	9.5
12 37 55.726	0.025	62 15 07.18	0.18	3.4	6.2	120.0	10.8
12 37 56.986	0.016	62 20 59.32	0.11	<2.1	16.0	221.0	15.4
12 37 59.523	0.016	62 06 26.62	0.11	<2.0	20.7	266.0	16.8
12 37 59.589	0.022	62 11 02.47	0.15	–	7.9	85.0	10.1
12 38 00.927	0.016	62 13 36.18	0.11	<2.0	17.3	190.0	13.2
12 38 01.315	0.023	62 13 32.08	0.16	–	7.2	79.7	10.0
12 38 01.434	0.025	62 11 46.03	0.18	–	6.2	68.0	9.8
12 38 01.754	0.018	62 21 47.85	0.12	<2.1	12.5	191.0	15.0
12 38 03.649	0.018	62 17 11.52	0.12	3.0	12.5	253.0	16.0
12 38 05.526	0.023	62 14 45.92	0.16	–	7.3	83.2	10.3
12 38 06.409	0.020	62 03 24.81	0.14	–	8.8	150.0	14.5
12 38 06.510	0.018	61 57 09.23	0.12	2.8	12.6	610.0	36.7
12 38 06.791	0.015	62 12 42.25	0.10	<2.0	44.3	1010.0	53.8
12 38 07.251	0.021	62 07 18.83	0.15	–	8.2	107.0	11.7
12 38 07.447	0.016	62 25 19.60	0.12	2.7	15.8	492.0	28.9
12 38 07.738	0.027	62 25 49.78	0.19	–	5.7	148.0	17.3
12 38 08.452	0.027	62 25 31.57	0.19	–	5.8	136.0	16.8
12 38 11.510	0.024	62 09 42.83	0.17	–	6.7	83.4	10.9
12 38 12.507	0.026	62 14 55.15	0.18	3.7	5.9	148.0	12.4
12 38 18.203	0.022	62 08 58.27	0.15	–	7.7	106.0	11.9
12 38 18.691	0.027	62 10 29.00	0.19	–	5.5	73.7	11.0
12 38 20.466	0.015	62 18 28.55	0.11	6.9	26.1	1800.0	93.0
12 38 21.778	0.022	62 17 06.43	0.15	2.4	7.9	152.0	13.4
12 38 23.765	0.020	62 07 07.62	0.14	–	9.3	148.0	13.9
12 38 25.712	0.016	62 28 13.73	0.11	2.7	17.7	876.0	49.3
12 38 26.205	0.024	61 58 03.14	0.17	–	6.8	259.0	25.3
12 38 28.237	0.028	62 18 23.73	0.20	–	5.2	98.3	13.0
12 38 28.544	0.019	62 07 36.58	0.13	<2.2	10.0	165.0	14.6
12 38 29.392	0.018	62 16 49.28	0.12	<2.1	12.3	193.0	15.1
12 38 29.863	0.024	62 10 16.40	0.17	–	6.8	105.0	12.6
12 38 30.192	0.016	62 14 01.15	0.11	2.4	20.4	368.0	21.6
12 38 30.630	0.015	62 18 21.30	0.11	2.9	26.8	601.0	32.5
12 38 30.763	0.027	62 23 17.61	0.19	–	5.6	134.0	16.9
12 38 37.038	0.021	62 03 56.12	0.15	3.3	8.3	304.0	21.5

12 38	41.896	0.024	62 22	34.68	0.16	5.2	6.9	357.0	24.3
12 38	54.957	0.028	62 11	38.26	0.19	–	5.4	159.0	16.3
12 38	55.385	0.027	62 12	32.38	0.19	3.7	5.7	278.0	19.9
12 38	59.502	0.026	62 05	42.77	0.19	–	5.8	216.0	20.6
12 39	02.591	0.015	62 02	11.54	0.11	<2.0	26.9	1410.0	74.0
12 39	07.411	0.022	62 15	40.66	0.15	5.7	7.9	557.0	32.4
12 39	11.741	0.017	62 22	17.41	0.12	2.7	13.9	963.0	53.3
12 39	14.388	0.034	62 08	59.80	0.24	–	5.5	171.0	20.5
12 39	14.969	0.018	62 14	58.17	0.13	3.4	11.2	475.0	29.9
12 39	21.841	0.022	62 16	00.19	0.15	–	7.8	149.0	21.5
12 39	27.465	0.027	62 06	58.72	0.19	–	5.5	309.0	28.5
12 39	31.546	0.016	62 15	55.90	0.11	2.6	16.2	807.0	46.6

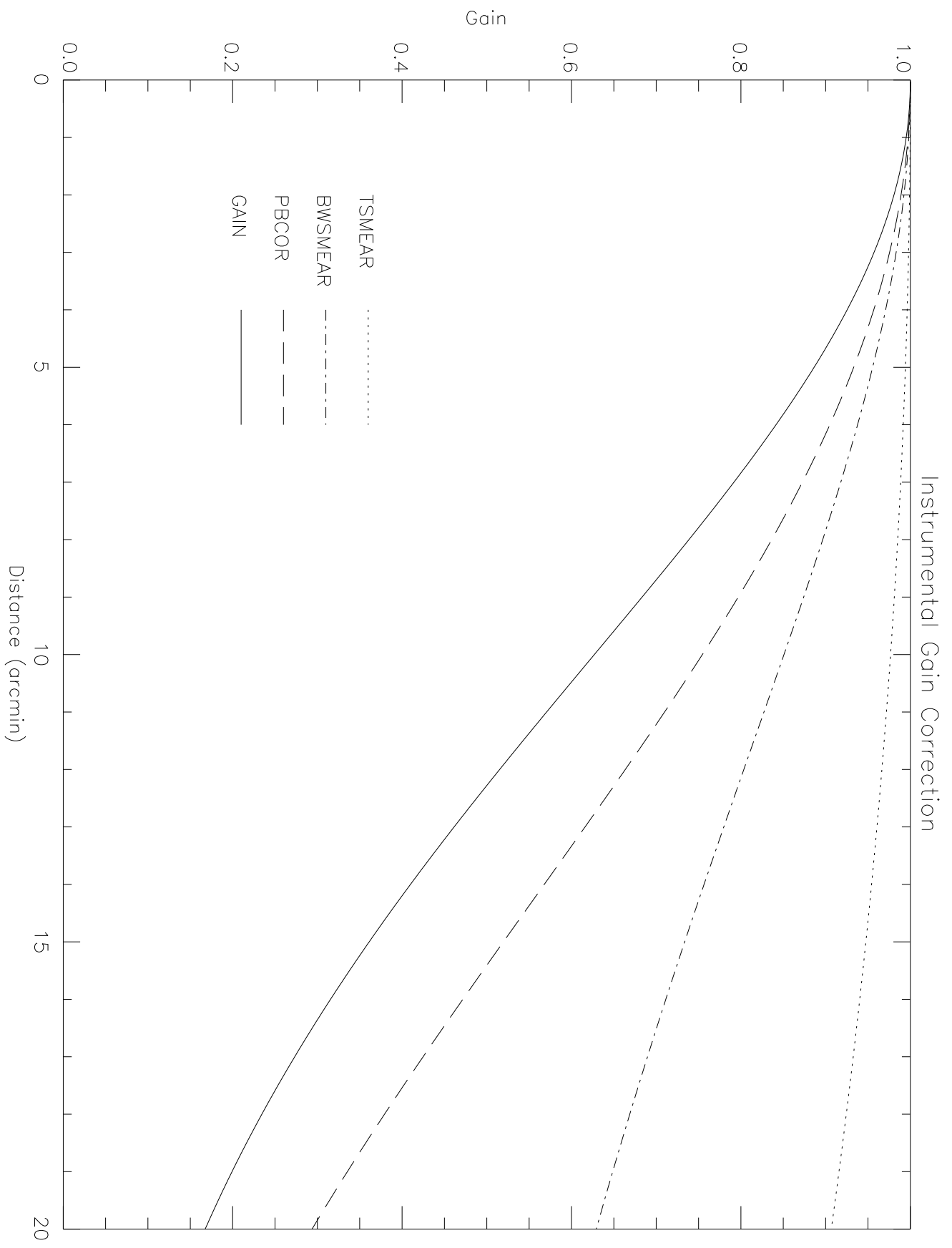


Table 3
1.4 GHz Source Count

Bin	$\langle S_{1.4} \rangle$	Area	dN/dS	Corr.	n/n _o
μJy	μJy	arcmin ²	ster ⁻¹ Jy ⁻¹	Factor	
40-67	55.4	232	9.4×10^{10}	1.3 ± 0.1	1.6 ± 0.4
67-82	73.7	421	9.3×10^{10}	1.1 ± 0.1	3.2 ± 0.5
82-102	91.4	519	5.7×10^{10}	1.0	3.0 ± 0.4
102-138	116	654	2.5×10^{10}	1.0	2.6 ± 0.4
139-203	162	872	1.1×10^{10}	1.0	2.6 ± 0.4
204-354	249	1067	3.7×10^9	1.0	2.8 ± 0.4
357-2100	512	1120	3.0×10^8	1.0	3.8 ± 0.5

1.4 GHz Angular Size Distribution

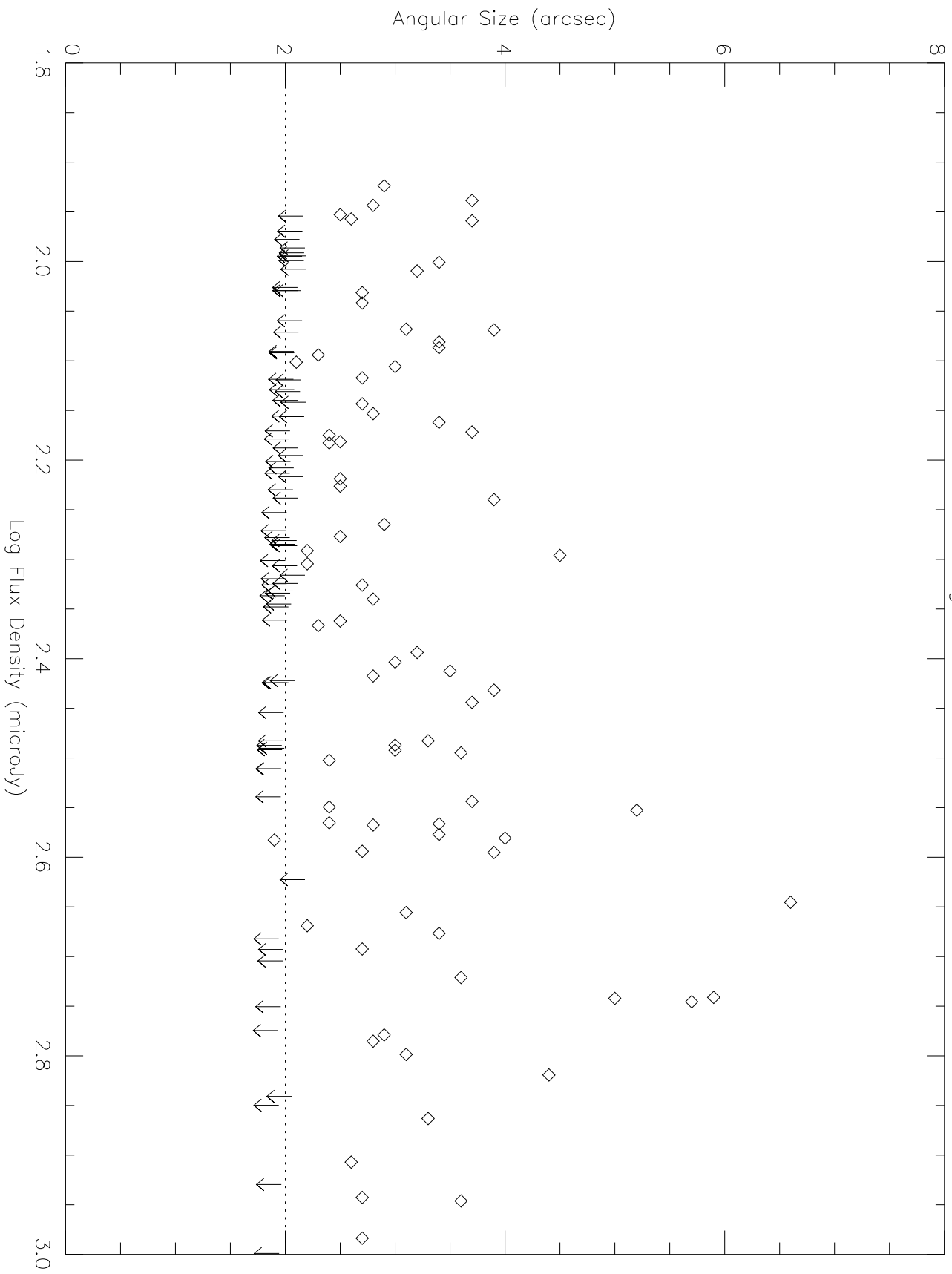


Table 4

Angular Correlation Function

Bin	$w(\theta)$	N_{DD}
arcmin		
0.0-0.1	-0.42 ± 0.28	12
0.1-0.3	-0.27 ± 0.17	21
0.3-0.8	0.12 ± 0.17	166
0.8-1.8	0.25 ± 0.05	804
1.8-3.8	0.22 ± 0.06	3236
3.8-7.8	0.19 ± 0.05	11705
7.8-16	0.06 ± 0.06	29505
16-40	-0.15 ± 0.03	23186

Median Angular Size for Submillijansky Population

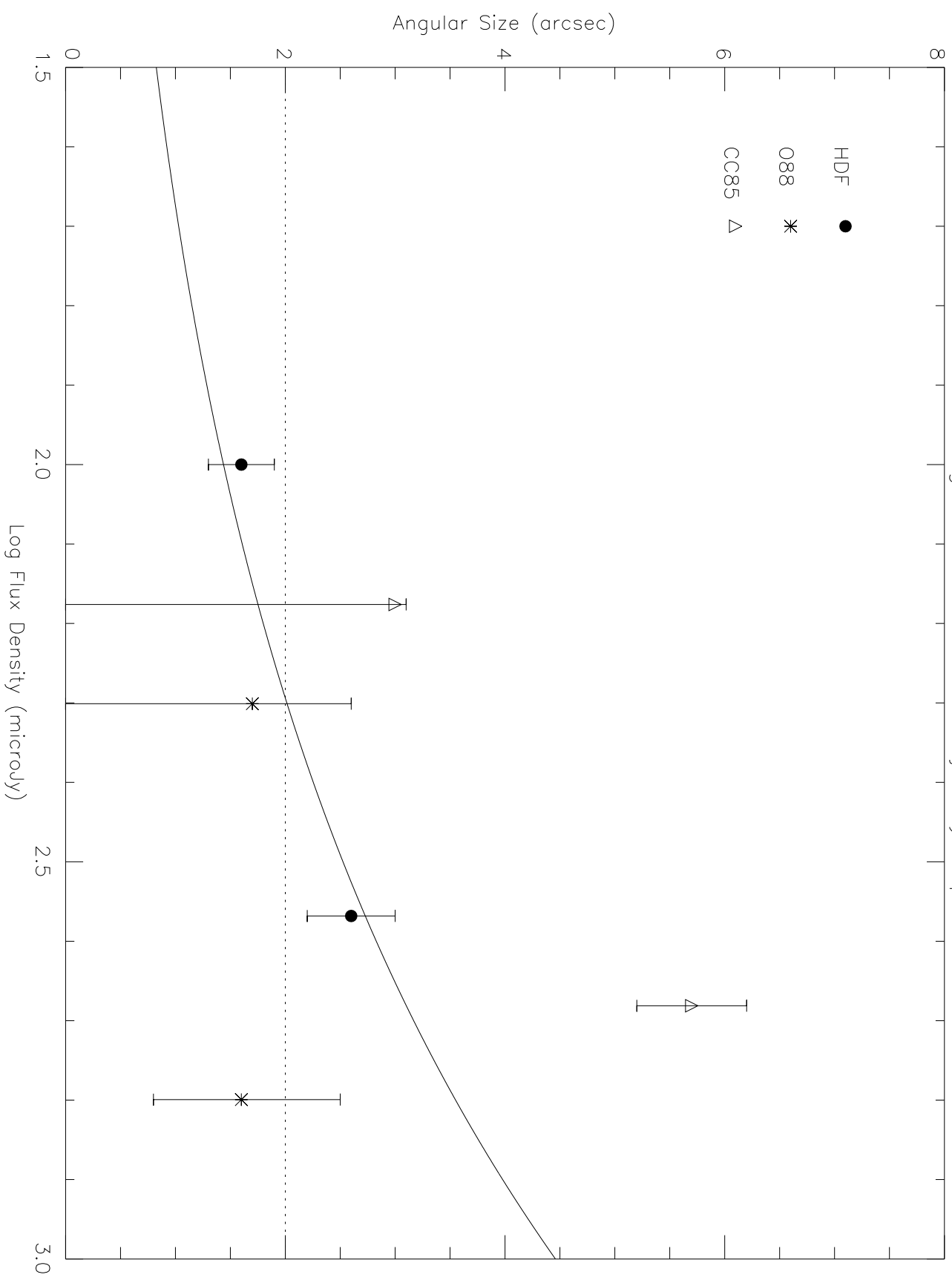


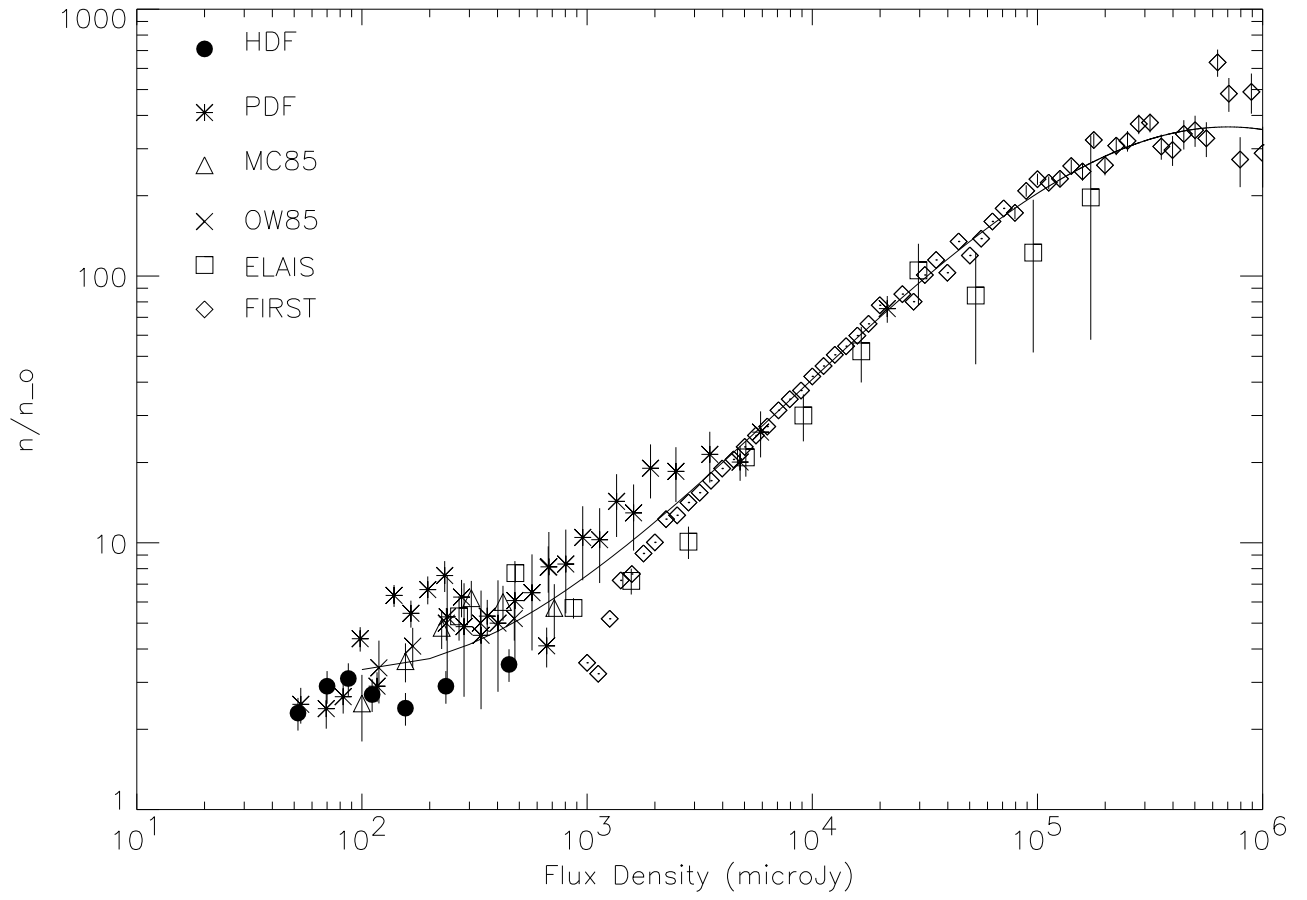
Table 5: Spectral Indices for HDF Radio Sample

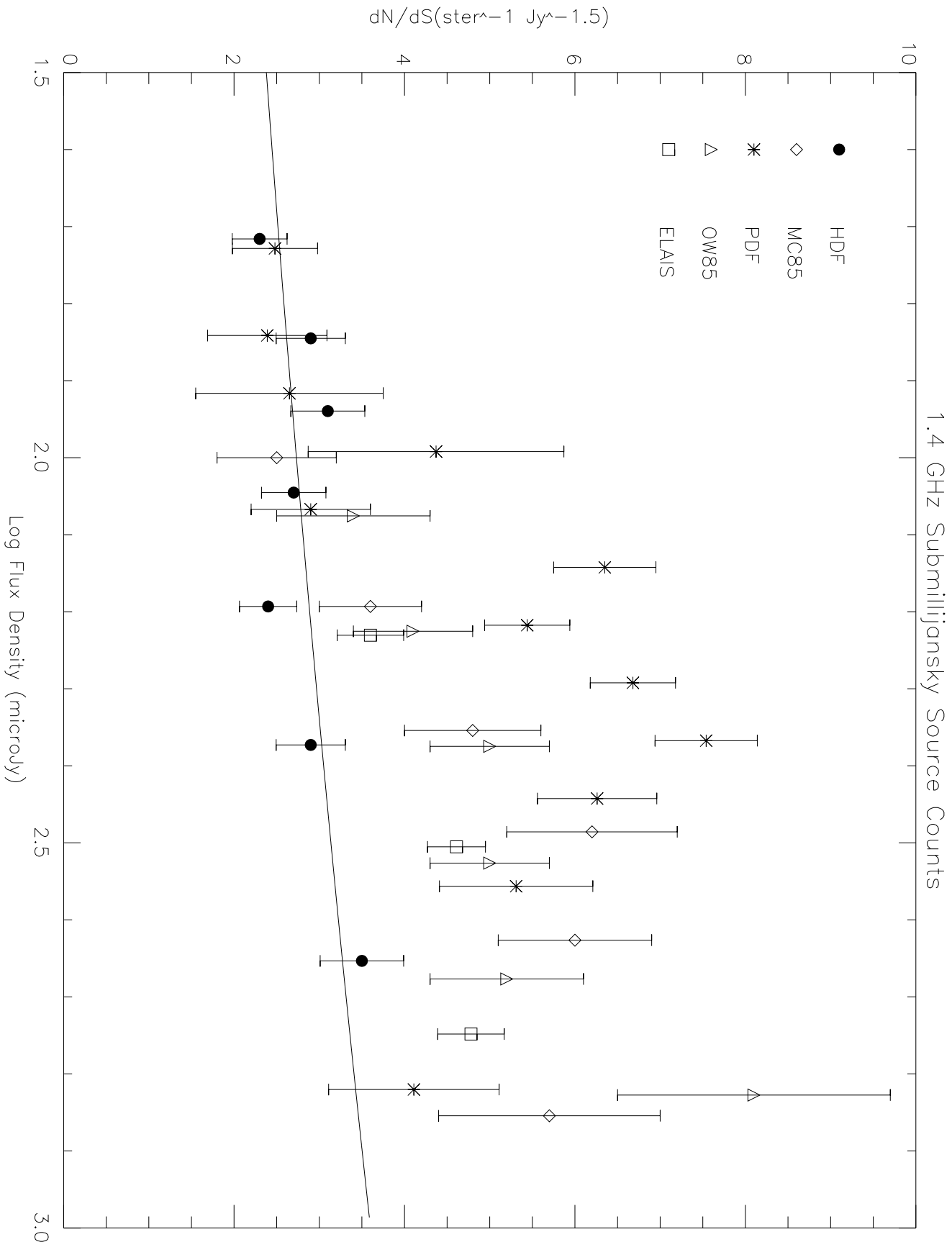
Source	$S_{8.5}$	$S_{1.4}$	α	θ_{las}	sample
VLAJ123600+621047	<51.0	125.2	>0.50	<2.1	l
VLAJ123606+620951	<70.4	191.0	>0.56	1.9	l
VLAJ123608+621035	123.0	233.0	0.36±0.08	<2.0	h, l
VLAJ123608+621552	90.5	52.9	-0.24±0.10	-	h, l
VLAJ123612+621140	<24.0	119.0	>0.89	2.4	l
VLAJ123618+621540	<71.4	190.0	>0.55	<2.0	l
VLAJ123618+621550	<47.0	145.0	>0.63	<2.0	l
VLAJ123619+621252	<21.8	91.4	>0.80	2.0	l
VLAJ123620+620844	218.00	220.0	0.01±0.07	<2.1	h, l
VLAJ123621+621108	<15.0	69.6	>0.86	-	l
VLAJ123621+621708	<58.7	159.0	>0.56	<2.0	l
VLAJ123622+621544	<24.6	72.5	>0.60	2.0	l
VLAJ123623+621642	153.0	475.0	0.63±0.07	<1.9	h, l
VLAJ123629+621045	<15.4	71.6	>0.86	-	l
VLAJ123631+620957	<26.7	156.0	>0.99	1.8	l
VLAJ123632+621105	21.8	<23.0	<0.10	<3.5	h
VLAJ123632+620800	<36.9	104.0	>0.58	2.2	l
VLAJ123633+621006	<8.4	48.2	>0.98	-	l
VLAJ123634+621435	14.0	<25.0	<0.32	-	h
VLAJ123634+621212	56.5	211.0	0.74±0.06	1.9	h, l
VLAJ123634+621241	52.6	198.0	0.74±0.06	2.0	h, l
VLAJ123635+621424	<14.3	69.7	>0.87	2.1	l
VLAJ123637+621135	17.5	<23.0	<0.20	<3.5	h
VLAJ123637+620852	<18.5	79.8	>0.82	-	l
VLAJ123638+621117	12.0	<25.0	<0.41	-	h
VLAJ123640+621010	29.2	64.5	0.44±0.15	2.1	h, l
VLAJ123640+621833	<73.5	307.0	>0.80	<2.0	l
VLAJ123642+621142	18.6	30.0	<0.27	<6.0	h
VLAJ123641+620948	<21.2	57.8	>0.56	-	l
VLAJ123642+621331	79.9	432.0	0.94±0.06	1.8	h, l
VLAJ123642+621545	53.6	131.0	0.50±0.07	2.0	h, l
VLAJ123644+621249	10.2	<23.0	<0.46	-	h
VLAJ123644+621133	752.0	1290.0	0.30±0.05	2.0	h, l
VLAJ123646+621448	24.7	112.0	0.84±0.12	2.0	h, l
VLAJ123646+621445	13.3	77.2	0.98±0.15	2.8	h, l
VLAJ123646+621404	190.0	177.0	-0.04±0.06	<2.0	h, l
VLAJ123646+621630	<17.3	312.0	>1.62	2.2	l

VLAJ123646+620833	<29.6	87.9	>0.61	-	l
VLAJ123646+621226	<9.5	72.3	>1.14	2.9	l
VLAJ123649+621312	14.0	51.0	0.72±0.15	<6	h, l
VLAJ123649+620737	113.0	310.0	0.56±0.07	<2.0	h, l
VLAJ123650+620844	<20.6	86.2	>0.80	-	l
VLAJ123651+621030	26.0	98.7	0.74±0.14	<2.1	h, l
VLAJ123651+621221	16.8	60.2	0.71±0.12	-	h, l
VLAJ123652+621444	185.0	148.0	-0.12±0.07	1.9	h, l
VLAJ123653+621139	15.1	60.0	0.77±0.12	-	h, l
VLAJ123654+621039	<8.0	48.2	>1.00	-	l
VLAJ123655+621311	12.3	<23.0	<0.26	-	h
VLAJ123656+620917	<24.9	67.0	>0.55	-	l
VLAJ123655+620808	<23.5	107.0	>0.85	<2.1	l
VLAJ123656+621207	<4.8	45.7	>1.32	-	l
VLAJ123656+621302	<6.8	60.3	>1.22	-	l
VLAJ123658+621455	15.3	<23.0	<0.20	-	h
VLAJ123659+621435	11.4	<25.0	<0.44	-	h
VLAJ123659+621832	317.0	502.0	0.26±0.07	<2.0	h, l
VLAJ123700+620909	66.7	326.0	0.89±0.12	<2.0	h, l
VLAJ123701+621146	29.5	97.7	0.67±0.08	2.2	h, l
VLAJ123702+621401	<10.0	41.4	>0.79	-	l
VLAJ123705+621153	<6.0	59.1	>1.27	-	l
VLAJ123707+621408	29.0	48.6	0.29±0.16	-	h, l
VLAJ123707+621121	<14.8	64.0	>0.82	-	l
VLAJ123708+621056	26.4	49.1	0.35±0.17	-	h, l
VLAJ123709+621246	19.5	<23.0	<0.10	<3.5	h
VLAJ123709+620837	122.0	64.8	-0.35±0.11	-	h, l
VLAJ123711+621331	31.1	108.0	0.69±0.13	<2.1	h, l
VLAJ123711+621325	<13.7	109.0	>1.16	-	l
VLAJ123713+621826	<101.4	527.5	>0.92	<1.9	l
VLAJ123714+620823	1060.0	1380.0	0.15±0.08	<1.9	h, l
VLAJ123716+621512	85.8	180.0	0.41±0.09	<2.0	h, l
VLAJ123716+621733	<77.2	302.0	>0.76	<2.0	l
VLAJ123717+620827	<15.7	62.6	>0.77	-	l
VLAJ123721+621130	630.0	383.0	-0.28±0.06	1.9	h, l
VLAJ123721+621346	<12.4	40.7	>0.66	-	l

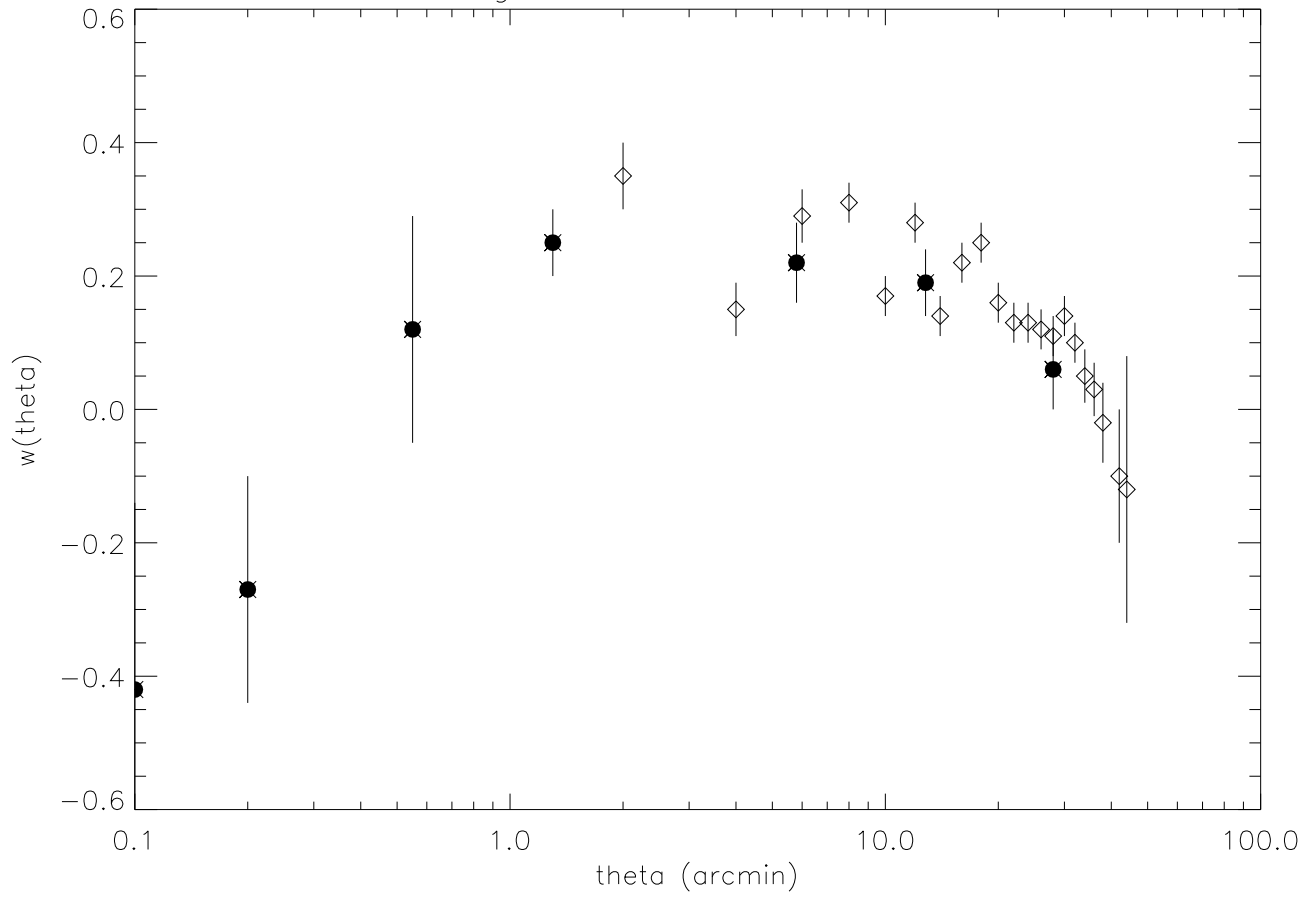
VLAJ123725+621128	530.0	5960.0	1.35 ± 0.06	0.8	h, l
VLAJ123730+621258	<27.1	112.2	>0.79	<2.1	l

1.4 GHz Source Counts

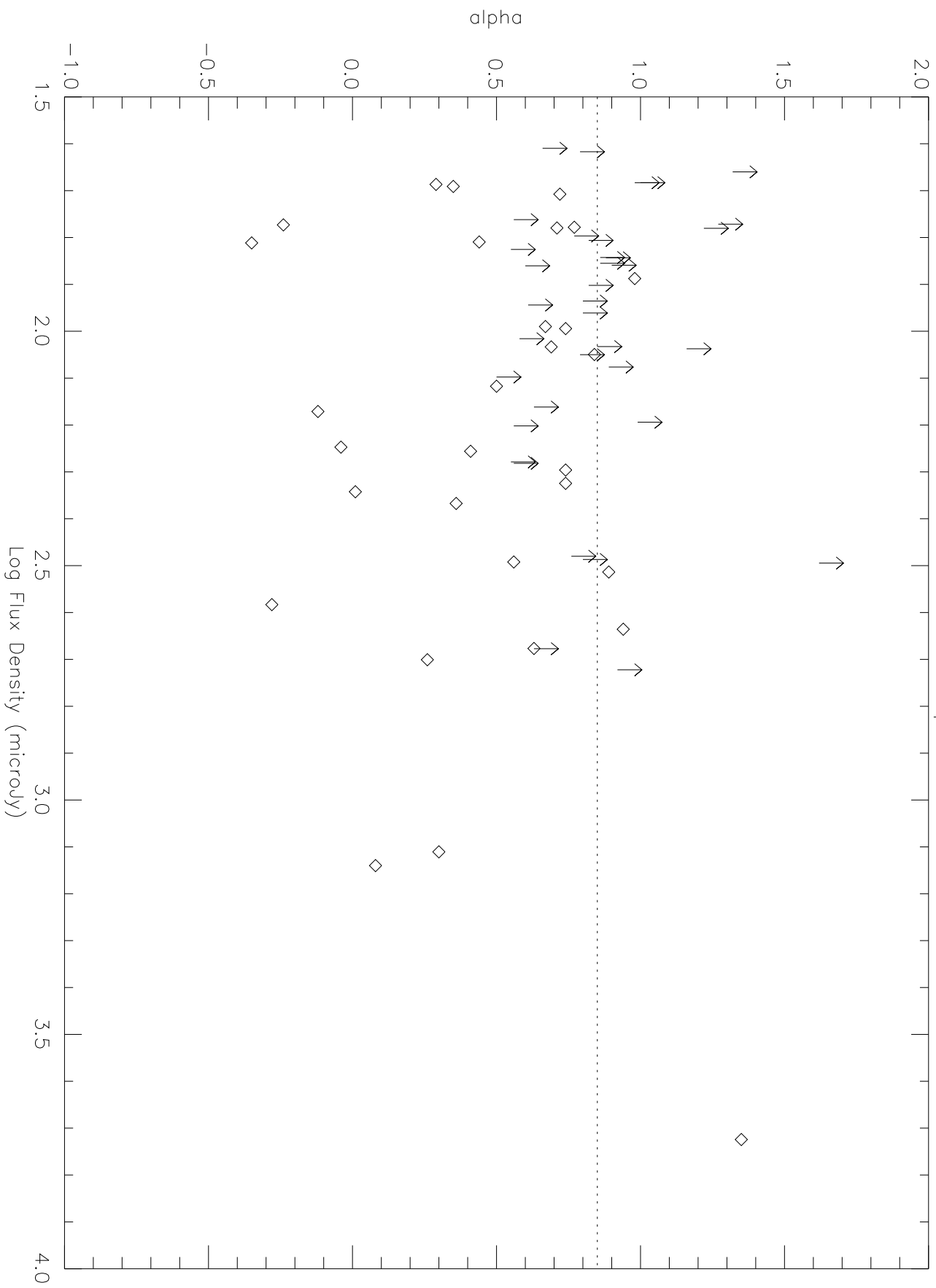




Angular Correlation Function



1.4 GHz Selected Spectral Indices



8.5 GHz Selected Spectral Indices

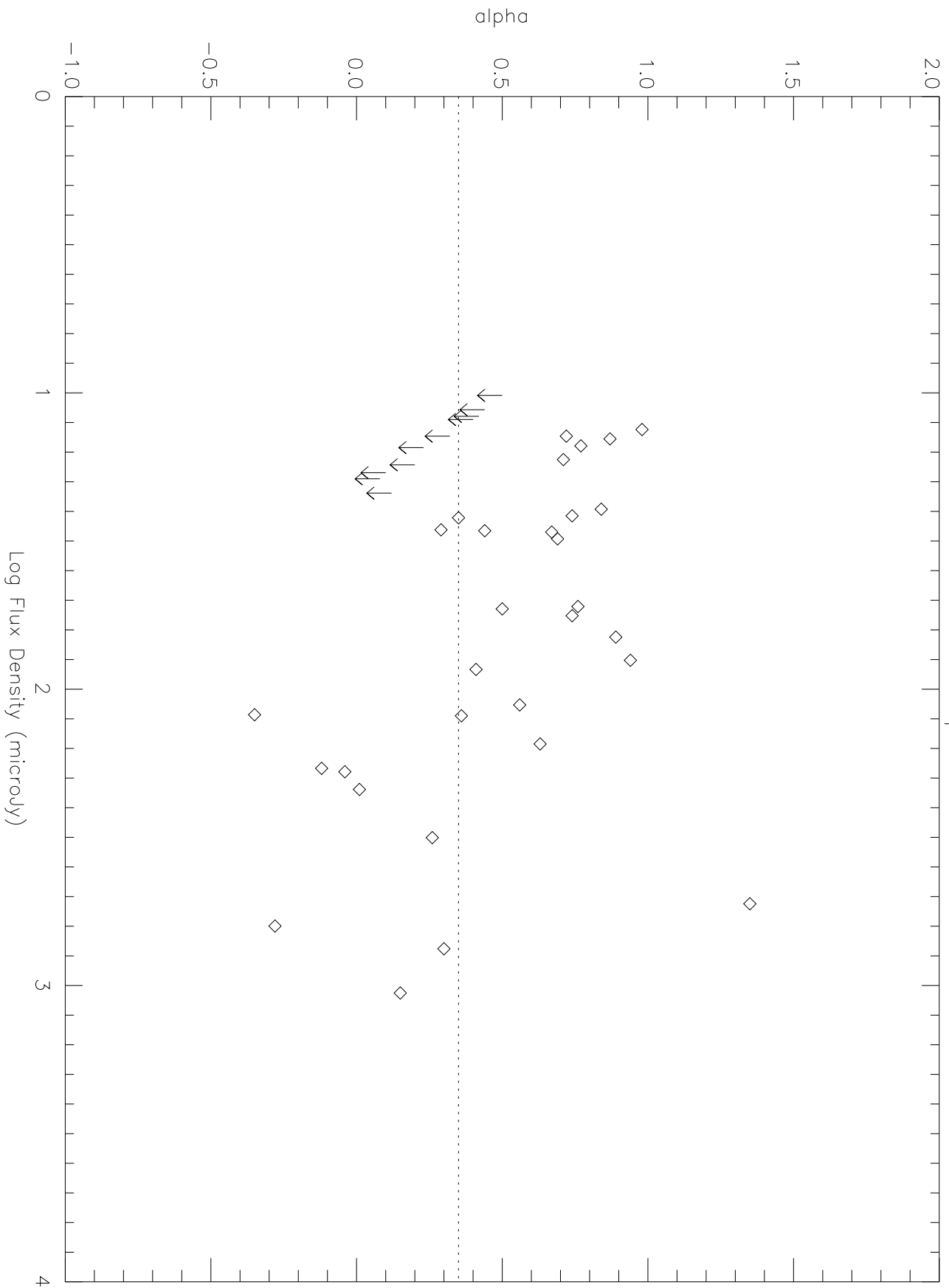


Table 1
VLA/Hubble Deep Field Imaging Parameters

Freq. (GHz)	Res. (arcsec)	Size (Pixels)	Pixel (arcsec)	Clean Comp	Pixel Max(μ Jy)	Pixel Min(μ Jy)	rms μ Jy/beam	Comp μ Jy
1.4	1.2	8192	0.4	160 000	30 000	-60	9.1	-
1.4	2.0	8192	0.4	160 000	35 000	-67	7.5	40.0
1.4	3.5	4096	0.8	80 000	51 000	-71	9.7	50.0
1.4	6.0	2048	1.6	16 000	63 000	-101	14.7	75
8.5	3.5	2048	0.4	20 000	630	-8.5	1.6	8.0